Magnetic Nanoparticles

by

Kenneth Adebayo, B.Sc.

A Thesis
Submitted to the Faculty of Graduate Studies
in Partial Fulfillment of the Requirements
for the Degree of

Master of Science

Department of Physics and Astronomy
University of Manitoba
Winnipeg, Manitoba

THE UNIVERSITY OF MANITOBA

FACULTY OF GRADUATE STUDIES

*****

COPYRIGHT PERMISSION

Magnetic Nanoparticles

BY

Kenneth Adebayo

A Thesis/Practicum submitted to the Faculty of Graduate Studies of The University of Manitoba in partial fulfillment of the requirement of the degree

Of

Master of Science

TABLE OF CONTENTS

LIST OF FIGURES

LIST OF TABLES

ACKNOWLEDGMENTS

I would like to express my sincere gratitude to my supervisor, Dr. Byron Southern. His help, stimulating suggestions, understanding, encouragement and personal guidance helped me in the research for and writing of this thesis. I would like to express my appreciation to my examinating committee members, Dr. Johan van Lierop and Dr. Georg Schreckenbach.

I would also like to thank Dr. Peter Blunden, Head of the Department of Physics and Astronomy, and the Departmental secretaries, Wanda Klassen and Susan Beshta for their support.

I feel a deep sense of gratitude for my late father and mother Mrs. Roseline Adebayo who formed part of my vision and taught me the good things that really matter in life. The happy memory of my father still provides a persistent insipration for my journey in this life.

I am grateful to my siblings Francis, Toyin, Bunmi and Ademola for their support. Lastly and most importantly, thanks be to God Almighty for His blessings and abundant grace.

This research has been supported and funded by the Natural Sciences and Engineering Research Council (NSERC) and the University of Manitoba Provincial Graduate Scholarship program.

ABSTRACT

We consider a simple model of maghemite nanoparticles and study their magnetic properties using Monte Carlo methods. The particles have a spherical geometry with sizes ranging from 3 nm to 8 nm. The interior of the particles consists of core spins with exchange interactions and anisotropy given by the values in the bulk material. The outer layer of the particles consists of surface spins with weaker exchange interactions but an enhanced anisotropy. The thermal behaviour of the total, core and surface magnetizations are calculated as well as the hysteresis loops due to the application of an applied field. The effect of the surface anisotropy on the blocking temperature, the coercive and exchange bias fields is studied.

Chapter 1

INTRODUCTION

This thesis deals with the modeling and simulation of the magnetic properties of nanoscale magnetic systems. Nanomagnetism refers to the underlying magnetic behaviour of nanostructured $(1-100\text{nm})$ systems. It focuses on the magnetic behaviour of individual building blocks of nanostructured systems as well as on combinations of individual building blocks that display collective magnetic phenomena. A fundamental understanding of nanomagnetism will lead to the development of integrated systems with complex structures and architectures that possess new functionalities. Proximity effects allow multi-component composites to behave as new materials that embrace properties that are often mutually exclusive and thus not found in single component systems. Competing interactions and the presence of low-lying energetic states and quantum fluctuations help create the complexity that gives rise to unanticipated phenomena in magnetic nanosystems.

Understanding these properties requires the utilization of high-performance computing to simulate complex behavior. Magnetism in confined geometries is an area of research that will surely produce much new science and many applications in the next twenty years. Confined systems that exhibit novel properties often consist of dissimilar materials that include at least one or more magnetic component (ferromagnetic, antiferromagnetic, etc.). It is necessary to apply theoretical and numerical approaches to study the effects of these unusual geometries.

Magnetism and magnetic materials have been traditionally studied with phe-

nomenological models. These models either work well or must be supplemented by new terms in the model to account for unexplained effects. Such an approach has limitations. The model may not be able to explain characteristics that depend on the details of the system at the nanoscale and may not have predictive capabilities. Magnetic properties at interfaces and surfaces, which make up a large fraction of nanostructured and confined materials, are quite different from the bulk systems upon which many simple models are built.

Fundamental to understanding the magnetic behaviour is the evolution of the magnetism as the structural scale descends from the bulk to the nanoscale. Due to reduced symmetry, the magnetic anisotropy can be orders of magnitude larger than in the bulk. This result can lead to magnetic frustration and reorientation of the magnetization at the surface and interface. Furthermore, interfaces between dissimilar materials can change their individual properties. For example, when in contact with an antiferromagnet, the properties of a ferromagnet change dramatically; the coercive field is enhanced and the magnetization curve can become asymmetric showing the exchange bias effect. In nanoscale magnetic particles, interface effects are expected to be even more significant as the interface region is a dominant part of the entire structure. Understanding the complex atomic spin structure of magnetic nanostructures using computational approaches is thus essential to the mastering of nanomagnetism itself.

The organization of the thesis is as follows. Chapter 2 is a brief introduction to magnetism and magnetic interactions. The quantum mechanical origins of exchange interactions are discussed. The magnetic properties of both bulk magnetic materials and small magnetic particles are described. Chapter 3 reviews the experimental properties of maghemite nanoparticles and decribes the model that will be used to study the magnetic properties. Monte Carlo methods are described in chapter 4. Several different algorithms are discussed in detail. Chapter 5 presents the results of the Monte Carlo simulations for particles of different sizes and with different anisotropy

constants. Chapter 6 summarizes the main results and describes possible future work on this topic.

Chapter 2

MAGNETISM

2.1 Exchange Interactions

Many bulk materials have an *ordered* magnetic structure at low temperatures [1, 2, 3, 4, 5]. The term *ordered* means that in the absence of an externally applied magnetic field, the mean magnetic moment of at least one of the atoms in each unit cell of the material is non-vanishing at a finite temperature. The simplest case corresponds to ferromagnets such as Fe, Ni and Co where the mean magnetic moments of all the atoms have the same orientation below a critical temperature called the Curie temperature, T_C. In other materials, the mean magnetic moments compensate each other within each unit cell and the material consists of magnetic sublattices below a critical temperature called the Néel temperature, T_N. These materials are referred to as antiferromagnets. A third type of magnetic order occurs in ferrites where the magnetic sublattices do not compensate each other leading to a net mean magnetic moment below a critical temperature T_C. These are called ferrimagnets. Above these critical temperatures, the magnetic order disappears abruptly and the mean magnetic moments of the atoms are zero. This high temperature state is referred to as paramagnetic. These magnetic states are shown in Fig. 2.1.

The magnetic order in materials is due to a correlation between the directions of the electron spins on individual atoms. This correlation is a purely quantum mechanical effect due to the indistinguishability of identical particles and the fact that electrons obey Fermi-Dirac statistics. The effect is called the exchange interaction [6, 7] and results in the energy of the system depending on the total electron spin.

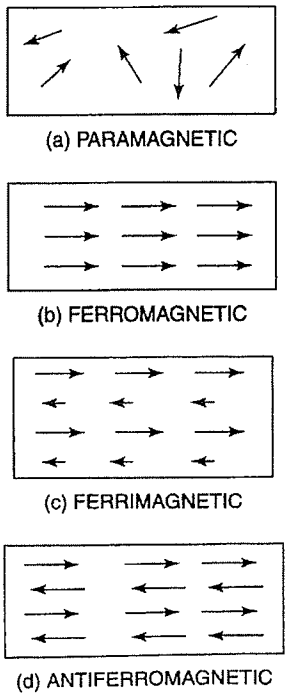

Figure 2.1: Various magnetic states

As a simple example, consider the hydrogen molecule consisting of two electrons and two protons which interact electrostatically. The Hamiltonian of the system is

$$H = \frac{p_1^2 + p_2^2}{2m} + e^2 \left(\frac{1}{r_{ab}} + \frac{1}{r_{12}} - \frac{1}{r_{a1}} - \frac{1}{r_{a2}} - \frac{1}{r_{b1}} - \frac{1}{r_{b2}} \right) \tag{2.1}$$

where p_1, p_2 are the electron momenta, m and e are the electron mass and charge, and $r_{\alpha,\beta}$ are the distances between particles α and β (1,2 refer to electrons and a, b refer to protons). The two protons are at a fixed distance r_{ab}. Since there are no interactions between the electron spins, the wave function ψ for the two electrons can be written as a product of space and spin wave functions

$$\psi(r_1\sigma_1, r_2\sigma_2) = \phi(r_1, r_2)\chi(\sigma_1, \sigma_2) \tag{2.2}$$

where σ_1, σ_2 are projections of the electron spins along a given axis. The wave function must be anti-symmetric with respect to the simultaneous interchange of the electron space and spin coordinates. Hence an antisymmetric space function is associated with a symmetric spin function and a symmetric space function is associated with an anti-symmetric spin function. The spin function χ is symmetric when the total spin of the electrons is unity (S=1) and anti-symmetric when S=0.

Hence

$$\begin{aligned} \psi(r_1\sigma_1, r_2\sigma_2) &= \phi_s(r_1, r_2)\chi_a(\sigma_1, \sigma_2) \quad S = 0 \\ &= \phi_a(r_1, r_2)\chi_s(\sigma_1, \sigma_2) \quad S = 1 \end{aligned} \tag{2.3}$$

where the subscripts a and s refer to anti-symmetric and symmetric functions, respectively. The symmetrized space wave functions are

$$\begin{aligned} \phi_s(r_1, r_2) &= \frac{1}{\sqrt{2(1+c^2)}}(\phi(r_{a1})\phi(r_{b2}) + \phi(r_{a2})\phi(r_{b1})) \quad S = 0 \\ \phi_a(r_1, r_2) &= \frac{1}{\sqrt{2(1-c^2)}}(\phi(r_{a1})\phi(r_{b2}) - \phi(r_{a2})\phi(r_{b1})) \quad S = 1 \end{aligned} \tag{2.4}$$

where

$$c = \int\int\int \phi(r_{a1})\phi(r_{b1})d^3r_1 = \int\int\int \phi(r_{a2})\phi(r_{b2})d^3r_2 \tag{2.5}$$

is the overlap of hydrogenic wave functions centered on the two protons.

The energies of the molecule corresponding to $S = 1$ and $S = 0$ are

$$\begin{aligned} E_{\uparrow\uparrow} &= \frac{A(r_{ab}) - B(r_{ab})}{\sqrt{1-c^2}} \quad S = 1 \\ E_{\uparrow\downarrow} &= \frac{A(r_{ab}) + B(r_{ab})}{\sqrt{1+c^2}} \quad S = 0 \end{aligned} \tag{2.6}$$

where A and B involve integrals over the electrostatic terms which depend on the separation of the two protons. Hence the Hamiltonian can be expressed as

$$H = -J(r_{ab})s_1.s_2 + E(r_{ab}) \tag{2.7}$$

where the first term depends on the relative orientation of the spins and the second term is independent of the spins. Since electons have spin $\frac{1}{2}$, the eigenvalues of the spin term are

$$s_1.s_2 = \frac{S(S+1)}{2} - \frac{3}{4} \tag{2.8}$$

and thus the Hamiltonian has eigenvalues $E_{\uparrow\uparrow}, E_{\uparrow\downarrow}$ if we set

$$\begin{aligned} J(r_{ab}) &= E_{\uparrow\uparrow} - E_{\uparrow\downarrow} \\ E(r_{ab}) &= \frac{3}{4}E_{\uparrow\uparrow} + \frac{1}{4}E_{\uparrow\downarrow} \end{aligned} \tag{2.9}$$

$J(r_{ab})$ is the exchange interaction which depends on the relative orientation of the electron spins. The exchange Hamiltonian was first obtained by Dirac[6] and is written

$$H_{ex} = -\sum_{i<j} J_{ij} s_i.s_j \tag{2.10}$$

where the sum is over nearest neighbour ions. This form is referred to as the Heisenberg Hamiltonian.

The exchange interaction is a consequence of the symmetrization requirements imposed on the wave function by quantum theory. In ferromagnets the exchange interaction J_{ij} is positive favouring a parallel alignment of spins whereas in antiferromagnets it is negative favouring an anti-parallel alignment. In ferrimagnets the exchange interaction can be of mixed sign. The magnitude of the exchange interaction is quite large due to its electrostatic origin and is responsible for magnetic order above room temperature. The exchange interaction described above is due to the overlap of the electron wave functions of the neighbouring ions and is called direct exchange. Other types of exchange occur in ionic solids and metals. The superexchange interaction takes place in ionic solids[8, 9, 10, 11]. Here the magnetic ions are often separated by non-magnetic ions. This is the case in oxides, sulphides and halides of transition metals. The magnetic ions are located at distances too great for their 3d wave functions to overlap. As an alternative, the exchange interaction is mediated by the non-magnetic ion. This interaction is active over short distances only. In metals

there can be a long ranged indirect exchange interaction mediated by the conduction electrons[12].

In addition to the exchange interaction, there are also the purely magnetic dipole interactions between magnetic moments of the atoms as well as the interaction of the magnetic moments with the electric field of the lattice (spin-orbit interaction). These latter interactions are relativistic in origin and hence are smaller than the exchange term. However they still play an important role since they lead to the appearance of an anisotropy energy.

2.2 *Vector Model of Atoms*

The magnetic moments of the individual atoms are due to both the orbital and spin motion of the electrons and the interaction between them. These angular momenta combine to form the total angular momentum $\vec{J} = \vec{L} + \vec{S}$. The total orbital and spin angular momentum of an atom are

$$\begin{aligned} \vec{L} &= \sum_i \vec{l}_i \\ \vec{S} &= \sum_i \vec{s}_i \end{aligned} \tag{2.11}$$

where the summation is over all electrons. The resultants $\vec{L}$ and $\vec{S}$ are loosely coupled to form the resultant total angular momentum $\vec{J}$ described by the quantum number J. This type of coupling is called Russell-Sanders coupling and J can take the range of values $J = |L-S|, ..., (L+S-1), (L+S)$. These groups of energy levels are called multiplets. If $L \geq S$,then we have $2S+1$ multiplets whereas, if $L \leq S$, we have $2L+1$ multiplets. The splitting of the atomic energy levels into the different types of multiplet levels takes place as a result of the spin orbit interaction

$$\lambda \vec{L} \cdot \vec{S} \tag{2.12}$$

where λ is the spin orbit coupling constant which determines the multiplet spacing. Treating the angular momenta as classical vectors, we have $J^2 = L^2 + S^2 + 2\vec{L} \cdot \vec{S}$.

Replacing the magnitudes J^2, L^2 and S^2 by their quantum values, the Jth energy level is

$$\frac{\lambda}{2}\left[J(J+1) - L(L+1) - S(S+1)\right] \tag{2.13}$$

The projection of the total magnetic moment $\vec{\mu}$ of the atom on the total angular momentum $\vec{J}$ is given by $\vec{\mu} = -\frac{e}{2m} g_J \vec{J}$ where

$$g_J = 1 + \frac{J(J+1) + S(S+1) - L(L+1)}{2J(J+1)} \tag{2.14}$$

is called the Lande g-factor. Note that $g_J = 1$ for pure orbital motion ($S = 0$) and $g_J = 2$ for the spin only case ($L = 0$).

When the atom is placed in a magnetic field, the components of the magnetic moment parallel to the field have $2J + 1$ discrete values in each mulitplet. The ground (lowest energy) state of an atom is labelled by the values of L, S and J using spectroscopic notation. The letters $S, P, D, F, G, ...$ signify the value of $L = 0, 1, 2, 3, ...$ respectively. A pre-superscript to the capital letter gives the value of $2S + 1$ and a post-subscript denotes the J value. In order to determine the most stable spin and orbital arrangements, we may use Hunds rules which state:

- (i) $S = \sum m_{si}$ is the maximum allowed by the Pauli principle. For a given electronic configuration, the term with the maximum spin multiplicity has the lowest energy.

- (ii) For a given spin multiplicity the term with the largest value of $L = \sum m_{li}$ lies lowest in energy.

- (iii) The resultant L and S combine to form J:

  a) $J = |L - S|$ for a shell less than half filled,

  b) $J = L + S$ for a shell more than half filled.

The first and second rules are the consequences of electrostatic interactions between electrons.

2.3 *Magnetic Anisotropy*

In addition to magnetic fields, electrostatic fields are also able to split the $(2J+1)$-fold degeneracy of a mulitplet. Consider an atom with orbital angular momentum $L = 1$ which is located in a uniaxial crystalline electric field of two positive ions along the z-axis. In the case of the free atom, we have states $m_L = 1, 0$ which have identical energies and are degenerate. In the crystal lattice, the atom will have a lower energy when the electronic charge cloud is close to the positive ions than when it is aligned halfway between the positive charges. The crystalline electric field is able to orient the electronic charge cloud into an energetically preferred direction.

2.3.1 Crystal Fields

In most compounds, the magnetic ions form part of a crystalline lattice in which the magnetic ions are surrounded by other ions. The Coulomb interactions between each electron and all other charges are described by the electrostatic potential $V_k(\vec{r}_k)$. For the case of iron ions the $3d$ electrons are outermost and are more affected by such a potential. In the case of the rare-earth ions the 4f electrons are shielded by the $5s^2 5p^6$ shells and they are less affected. The electrostatic field experienced by the unpaired electrons of a given magnetic ion is called the crystal field. The $(2J + 1)$-fold degeneracy of the ion's ground state will be split in the presence of a crystal field as well as in a magnetic field.

The neighbouring atoms can be treated as point charges and the crystal field potential is

$$V_k(\vec{r}_k) = \sum_j \frac{Z_j e}{|\vec{R}_j - \vec{r}_k|} \tag{2.15}$$

where $Z_j e$ is the charge on the jth ion located at $\vec{R}_j$. The advantage of treating the neighbours as point charges is that the potential satisfies Laplace's equation and the

total energy H_{cf} may be expanded in spherical harmonics as

$$H_{cf} = \sum_i \sum_{n\ even} \sum_{m=-n}^{m=n} A_n^m r^n Y_n^m(\theta_i, \phi_i) \tag{2.16}$$

where A_n^m are the coefficients of this expansion which have values that depend on the crystal structure considered and determine the strength of the crystal-field interaction. The lowest order term is called a uniaxial anistropy and has the form

$$H_{cf} = -\sum_i K S_{iz}^2 \tag{2.17}$$

2.3.2 Zeeman effect

The Zeeman effect is the splitting of a spectral line into several components in the presence of a static magnetic field $\vec{H}_0$. The Zeeman energy is

$$H_{Zeeman} = -\sum_i \vec{\mu}_i \cdot \vec{H}_0 \tag{2.18}$$

This is analogous to the Stark effect which is the splitting of a spectral line into several components in the presence of an electric field.

2.4 Magnetic Properties of Bulk Materials

The critical temperature of iron is above 1000K but it can appear to be unmagnetized at room temperature. However, it can be easily magnetized by stroking it with a permanent magnet. We need to consider magnetic dipolar interactions in order to understand this phenomenon.

2.4.1 Domains

The interaction between two magnetic dipoles $\vec{\mu}_i$ and $\vec{\mu}_j$ has the form

$$H_{dip} = \sum_{i<j} \frac{1}{r_{ij}^3} [\vec{\mu}_i.\vec{\mu}_j - 3(\vec{\mu}_i.\hat{r}_{ij})(\vec{\mu}_j.\hat{r}_{ij})] \tag{2.19}$$

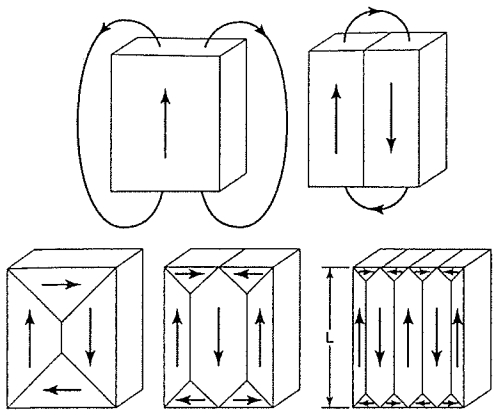

Figure 2.2: Domain formation

where r_{ij} is the separation of the two dipoles. This interaction is relatively weak compared to the direct exchange between neighbouring moments but it is long-ranged. The magnetic configuration of a macroscopic sample can be quite complicated. The ferromagnetic state which is favoured by the short range direct exchange does not minimize the dipolar energy. The dipolar energy can be reduced by dividing the sample into macroscopic domains as shown in Fig. 2.2. There is an energy cost for exchange at the domain boundaries but there is an overall energy gain. Hence the sample appears to be unmagnetized because the domains have different orientations.

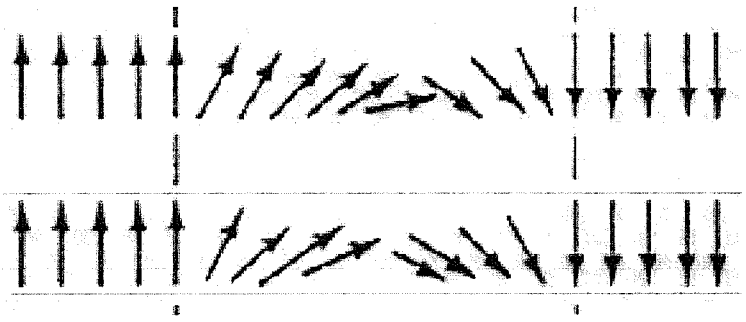

Figure 2.3: Domain wall

The wall separating domains[13] can be very sharp or broad depending on the exchange and anisotropy energies. For a single pair of spins, the exchange energy is $H_{ex} = -J\vec{s}_i.\vec{s}_j \sim -JS^2 + \frac{JS^2}{2}(\Delta\phi)^2$ where $\Delta\phi$ is the angle between the spins. For a very narrow wall, this is an abrupt change and the energy cost is $\frac{JS^2}{2}\pi^2$. However, a lower energy cost is obtained if the spins turn over gradually through a distance L with an angle π/L between adjacent spins as shown in Fig. 2.3. The energy cost is $\frac{JS^2}{2}L(\pi/L)^2$ and favours very wide walls. However, the anisotropy energy is increased by a wide wall since the spins deviate from the anisotropy axis within the wall. For a simple cubic lattice with lattice spacing a, the number of rows of atoms per unit area is $\frac{1}{a^2}$ and the exchange energy cost per unit area of domain wall is $\frac{JS^2}{2}\frac{\pi^2}{\delta a}$ where $\delta = La$ is the width of the wall. The anisotropy energy cost is $K\delta$ and the total energy cost is minimized for $\delta = (\frac{JS^2\pi^2}{2Ka})^{\frac{1}{2}}$ and depends on the ratio of exchange to anisotropy energies. Substituting this back into the energy cost per unit area, we have $\Delta E_{wall} = 2\pi(\frac{JS^2K}{2a})^{\frac{1}{2}}$.

2.4.2 Hysteresis and Coercivity

When a weak magnetic field is applied to such an unmagnetized sample, the domains reorient and grow as shown in Fig.2.4. For weak fields this process is reversible but for larger fields it becomes irreversible and a large field in the opposite direction is needed to demagnetize the sample. This phenomenon is called hysteresis and the field necessary to restore zero magnetization is called the coercive force. In order to characterize the magnetic properties, a field large enough to saturate the magnetization is applied and then it is reduced back to zero. The magnetization at this point is called the remanent magnetization. The field is then switched to the opposite direction until the state of zero magnetization is reached. The field value at this point is a measure of the coercivity of the sample.

The ease with which the magnetization of single crystal samples can be saturated also depends on the direction in which the field is applied when crystalline anisotropy

is present. Hence the measurement of hysteresis loops provides important information about the magnetic properties of bulk materials.

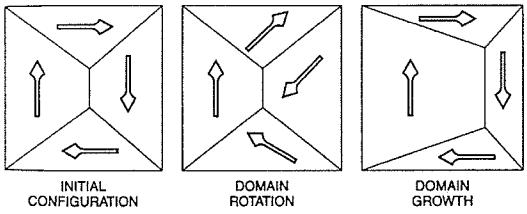

Figure 2.4: Domain rotation

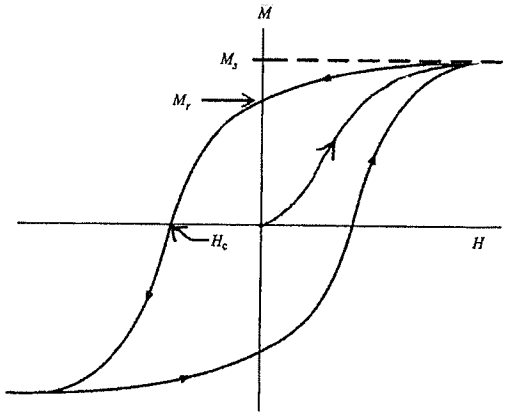

Figure 2.5: Hysteresis Loop

2.5 Small Magnetic Particles

The magnetism of small magnetic particles is dominated by two important features. The first is that there is an upper limit to the size of single domains and the second is that thermal energy can decouple the magnetization from the particle to give rise to the phenomenon of superparamagnetism.

2.5.1 Single domain Particles

Consider a large single crystal which is uniformly magnetized and hence forms a single domain. Surface charges will be formed on the ends of the crystal due to the magnetization and the single crystal itself is a source of magnetic field(demagnetizing field). There is an energy associated with the surface charge distributions called the magnetostatic energy. The crystal which is uniformly magnetized generates a large amount of stray magnetic field H. The field H has an energy that is expressed as

$$E_d = \frac{1}{2}\int H^2 dV \tag{2.20}$$

where the integral is over all space. This integral will become smaller for a crystal subdivided into two domains and even become much smaller if subdivided into more domains. This subdivision cannot continue indefinitely because the formation of a domain wall requires energy to be generated and maintained. A domain wall is an interface which separates magnetic domains and the magnetization has different directions on each side. Consider the boundary between two domains in which the magnetization changes by 180^0, described as a 180^0 wall (Fig. 2.2) and assume that the two domains are magnetized in easy directions. Since the spins within the walls are not aligned along a direction of easy magnetization, there some anisotropy energy associated within the wall and the exchange energy favours the spins parallel. Thus there is a competition between the anisotropy and exchange energies which makes the domain wall posses a finite width and surface energy. Exchange favours the wall to be as wide as possible whereas the anisotropy tends to make it as thin as possible. This interplay results in domain states being grain size dependent. As the crystal size decreases, a point will be reached where the crystal will no longer be able to accommodate a wall. Below this size the crystal contains a single domain. The single domain particle has high coercivity and remanence and is magnetically hard because the only way to change the magnetization of a single domain particle is to rotate the magnetization.

2.5.2 Superparamagnetism

As the size of the particle discussed above decreases further within the single domain range, a critical threshold is attained where the coercivity and remanence go to zero. A unixial single domain particle of volume V has a magnetic anisotropy energy given by

$$E_a = KV \sin^2(\theta) \tag{2.21}$$

where θ is the angle between $\vec{M}$ and the easy axis.

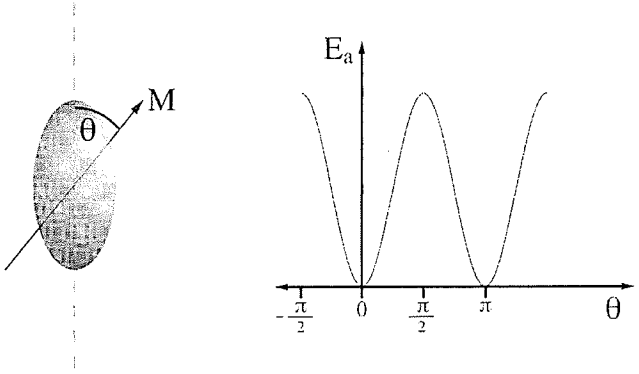

Figure 2.6: Single Domain Particle

The energy is a minimum at $\theta = 0, \pi$ and has a maximum at $\theta = \pi/2$ with an energy barrier KV as shown in Fig. 2.6. In the absence of an applied field and at low temperatures, the particle moment is trapped in one of the wells and moment is said to be blocked. At higher temperatures, thermal energy can induce fluctuations of the moment from well to well and the moment becomes unblocked as illustrated in Fig. 2.7.

The net magnetic moment will be zero in zero applied field and at high temperatures. Such particles whose magnetization fluctuates spontaneously are analogous to paramagnetic particles except that they possess magnetic moments which are much larger. These particles are said to exhibit superparamagnetism which was predicted

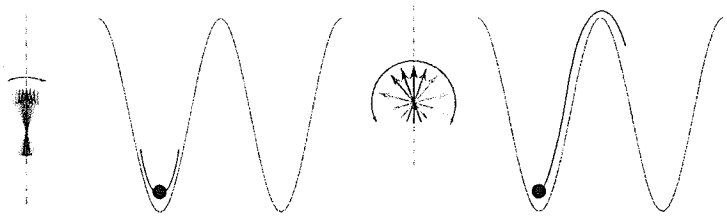

Figure 2.7: Blocked and unblocked moment

by Néel [14, 15].

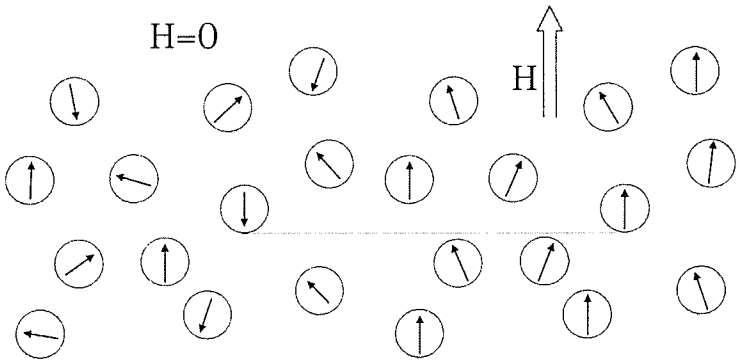

Figure 2.8: Superparamagnetism

The magnetic blocking temperature, T_B is the temperature below which the particle moment is blocked. T_B depends on the particle size and the timescale of measurement. In response to a change in applied field or temperature, a collection of single domain particles will approach an equilibrium value of the magnetization with a characteristic relaxation time τ

$$\frac{1}{\tau} = f_0 exp(-\frac{KV}{k_B T}) \tag{2.22}$$

where f_0 is an attempt frequency (10^9 sec^{-1}), T is the absolute temperature and k_B is Boltzmann's constant. Fig.2.9 shows a $ln - ln$ plot of the relaxation time versus inverse temperature. The slope is proportional to the particle volume V.

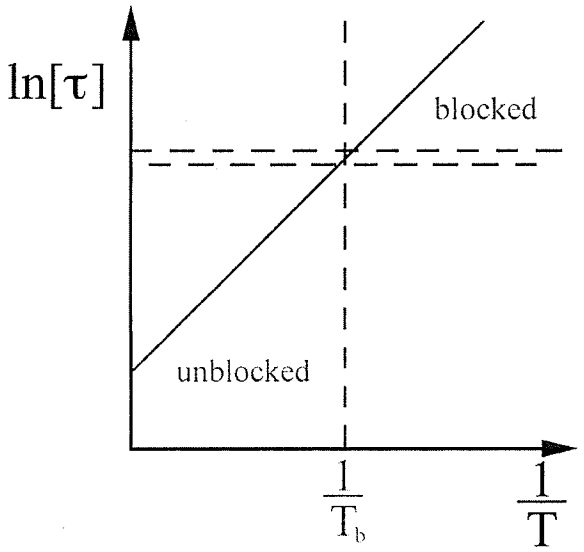

Figure 2.9: Blocking Temperature

Stoner and Wohlfarth[16] predicted a $T = 0$ coercivity of $\frac{2K}{M_s}$ for a particle with anisotropy constant K (the anisotropy is due to shape or the crystalline structure) and saturation magnetization M_s if the magnetization rotates coherently and the external magnetic field is applied in the direction of the easy axis. This theory marked the beginning for the development of magnets and magnetic recording materials. The magnetization is aligned parallel to the external magnetic field H in the absence of any anisotropy. For uniaxial anisotropy, there is an associated anisotropy energy

density

$$E = K\sin^2(\theta) - HM_s\cos(\phi - \theta) \tag{2.23}$$

where θ is the angle between M_s and the easy axis and ϕ is the angle between the applied field and the easy axis. Minimizing 2.23 with respect to θ we have

$$K\sin(2\theta) - HM_s\sin(\phi - \theta) = 0 \tag{2.24}$$

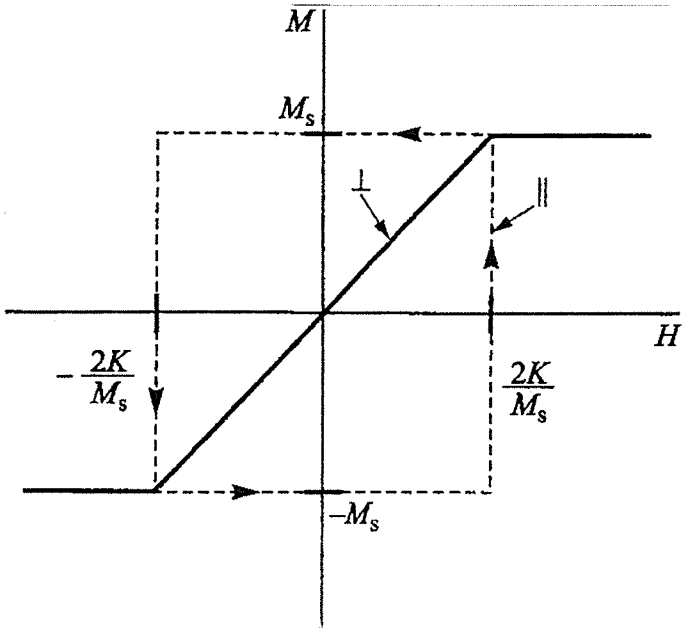

Figure 2.10: Hysteresis loops for fields perpendicular and parallel to the easy axis

In the case where $\phi = \pi/2$, the magnetization rotates towards the field direction as the field magnitude increases and is saturated when $H = \frac{2K}{M_s}$. This process is reversible and there is no hysteresis. For $\phi = 0, \pi$, the magnetization is along the easy axis but reversal of the field direction leads to a coercivity $H_c = \frac{2K}{M_s}$. This behaviour is shown in Fig.2.10. For other values of ϕ saturation does not occur in a finite field and the qualitative shape of the hysteresis loop is shown in Fig.2.11. This behaviour

would also describe a collection of single domain particles with random easy axis directions.

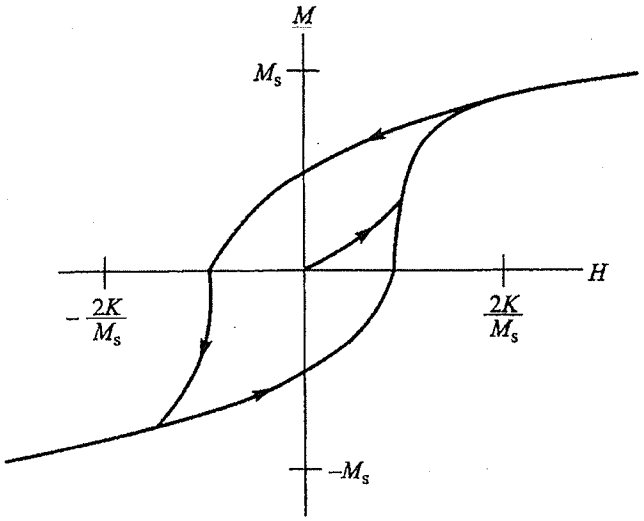

Figure 2.11: Hysteresis loop for a collection of uniaxial single domain particles with random easy axes

The temperature dependence of the coercivity can be described using (2.22) by replacing KV by the energy barrier ΔE in an applied field and setting $\Delta E = CT$ where C is a constant of order $25k_B$. This gives a relaxation time of approximately $10^2 s$ which exceeds measurement times by many orders of magnitude. Equation (2.24) has solutions $\theta = 0, \pi$ and $\cos(\theta) = -\frac{HM_s}{2K}$ and the energy barrier is $(\frac{H^2M_s^2}{4K} + K - HM_s)V$. Solving for the coercive field we find

$$H_c = \frac{2K}{M_s}\left(1 - \sqrt{\frac{T}{T_B}}\right) \tag{2.25}$$

where $T_B = \frac{4KV}{C}$. The coercivity vanishes at and above the blocking temperature T_B which clearly depends on the particle volume V and time scale constant C. The smaller the single domain particle or the longer the measurement time, the lower the value of T_B.

2.5.3 Magnetic Surface Anisotropy

An important difference between bulk magnetic materials and small particles is that the sites on the surface have a reduced symmetry. For this reason, the magnetic anisotropy at the surface differs from that in the bulk. Since the outward normal $\hat{n}_i$ to the surface is in the direction of missing neighbours, the surface anisotropy energy is taken to have the form

$$H_s = -K_s \sum_i (\vec{S}_i . \hat{n}_i)^2 \tag{2.26}$$

where K_s is the surface anisotropy constant. Positive values favour moment alignment perpendicular to the surface and negative values favour alignment tangential to the surface.

2.6 Exchange Bias

The phenomenon of exchange bias[17, 18] occurs in systems where an interface between ferromagnetic and antiferromagnetic phases occurs and the two phases are exchange coupled at the interface. This occurs in both thin films and in small particles when the systems are cooled in a field. If the ferromagnet has a higher ordering temperature $T_C > T_N$ than the antiferromagnet and the system is cooled to a temperature T such that $T_N < T < T_C$, the ferromagnet will be single domain. Further cooling below T_N will order the antiferromagnet with the moments at the interface oriented parallel to the ferromagnetic moments. If the field is removed at a lower temperature, the antiferromagnet will maintain the ferromagnetic moments along the original field direction. When a reverse field is applied, the coherent rotation of the ferromagnet is impeded by the exchange interaction at the interface and a shifted hysteresis loop is found. The left coercive force h_1 is larger in magnitude than the right coercive force h_2. The coercive and the exchange bias fields are defined as

$$H_c = \frac{h_2 - h_1}{2} \qquad (2.27)$$
$$H_{ex} = \frac{h_2 + h_1}{2}$$

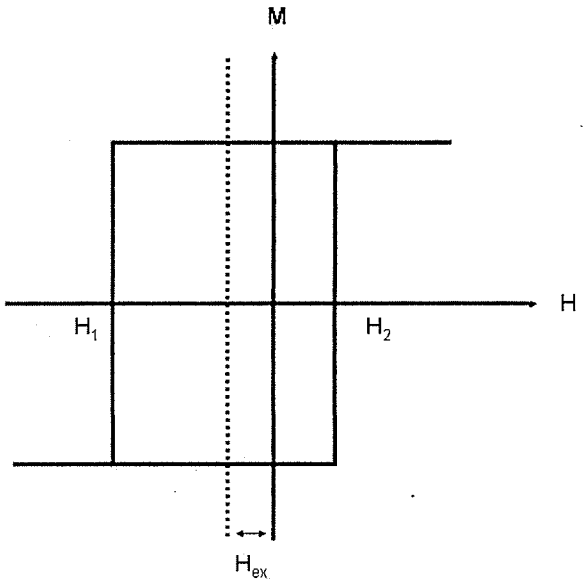

Figure 2.12: Biased hysteresis loop

Chapter 3

MAGHEMITE NANOPARTICLES

3.1 Experimental Facts

Bulk maghemite ($\gamma - Fe_2O_3$) is derived from magnetite (Fe_3O_4) which crystallizes in an inverse spinel structure with 8 Fe^{3+} ions located at tetrahedral sites (T), 16 Fe^{3+} ions in octahedral sites (O), and 32 O^{3-} ions per unit cell[19, 20, 21, 22, 23]. The lattice constant of the unit cell is .83 nm. Maghemite is formed by the removal of $\frac{1}{9}$ of the iron atoms and oxygen vacancies are distributed throughout the O sites to ensure charge neutrality. Hence there are $16 - \frac{24}{9} = \frac{40}{3} Fe^{3+}$ atoms on the O sites in a unit cell. The ground state configuration of the Fe^{3+} ion is ${}^6S_{\frac{5}{2}}$ which has $S = \frac{5}{2}, L = 0$ and $g_J = 2$. Competing superexchange interactions between the Fe^{3+} T and O sites leads to a ferrimagnetic ordering in the bulk material at $1020K$. The moments on the T and O sites are anti-parallel and the net moment per iron atom is $(\frac{\frac{40}{3}-8}{\frac{40}{3}+8})5\mu_B = .25 g_J S \mu_B = 1.25\mu_B$.

The magnetic properties of nanoparticles are greatly influenced by surface effects[24, 25] and their importance increases as the size of the particle decreases. With decreasing size, surface effects lead to a decrease of the ordering temperature and an enhanced surface anisotropy which differs significantly from that of the particle core. Recent experiments[26] on dilute suspensions of mono-disperse $\gamma - Fe_2O_3$ nanoparticles with an average diameter of 7 nm have suggested that the particles block at a temperature $T_B \sim 20K$ which is much lower than that where the core develops ferrimagnetic order. Below T_B the particles exhibit enhanced coercivity and exchange bias.

With decreasing size, the average magnetic coordination number of a $\gamma - Fe_2O_3$

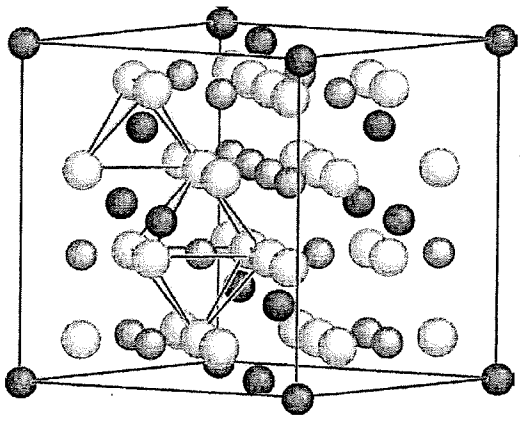

Figure 3.1: Unit cell of maghemite showing the oxygen ions (white) and the Fe^{3+} ions at the O (gray) and T (black) sites. Lattice constant is $.83nm$.

crystallite is significantly reduced, and finite-size effects become significant. A single-domain magnetic structure occurs, and the large number of magnetic ions in the unit cell make this system sensitive to vacancies distributed throughout the octahedral sites and especially at the surface. This leads to a magnetic roughness which can be thought of as an effective surface magnetocrystalline anisotropy that is different from the magnetocrystalline anisotropy of the nanoparticle single domain core. The single-domain ferrimagnetic core of the $\gamma - Fe_2O_3$ nanoparticle is magnetically ordered at a much higher temperature than the surface spins. Therefore, a preferred orientation can be imposed on the surface spins by field-cooling with a field large enough to align the particles cores. Field-cooling must occur from a temperature above that where the surface spins freeze into a spin-glass configuration. With the $\gamma - Fe_2O_3$ nanoparticle magnetism in this configuration, the single-domain core will experience the field generated by the frozen surface spins that are aligned by the field-cooling, and exchange coupling between the core moments and surface spins occurs. This exchange coupling is most easily observed by the resulting offset from zero field of the hysteresis loop, i.e., an exchange bias field (H_{ex}).

At low temperatures where the single-domain $\gamma - Fe_2O_3$ cores are in a blocked configuration and the thermal energy is not large enough to enable the nanoparticle moment to fluctuate about its easy axis (where we have assumed that the core magnetic anisotropy is uniaxial in nature), the temperature dependence of H_{ex} should mirror that of the surface spins and provide insight into their evolution. Upon warming, the single-domain cores of the nanoparticles will become unblocked just above the blocking temperature, T_B. Single-domain moments will now fluctuate about their easy axis undergoing superparamagnetic 180^0 moment flips. However, the magnetocrystalline anisotropy constant of fine-particle $\gamma - Fe_2O_3$ is $K = 1 - 2.5 \times 10^5\ erg\ cm^{-3}$[1] and thus a sub-10 nm diameter nanoparticle will have a rather large energy barrier to overcome that is associated with its superparamagnetic fluctuations.

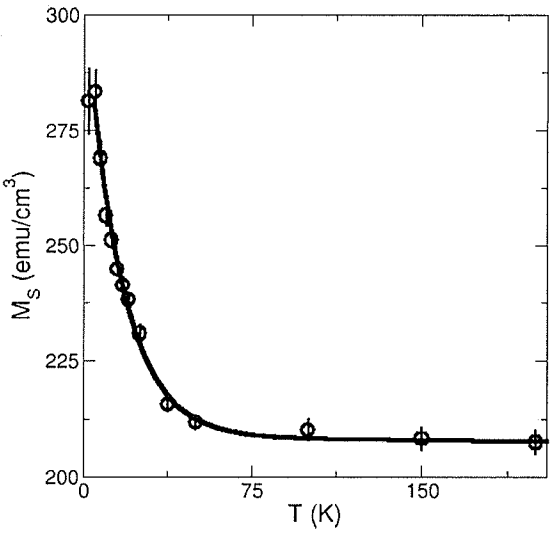

Figure 3.2: Saturation magnetization M_s of $\gamma - Fe_2O_3$ as a function of temperature.

A prominent feature of the $7nm$ $\gamma - Fe_2O_3$ particle nanomagnetism is the unique temperature dependence of the saturation magnetization, M_s, shown in figure 3.2. The effect of surface spin freezing in the $\gamma - Fe_2O_3$ nanoparticles displayed by $M_s(T)$ in figure 3.2 is well described by the phenomenological description using a modified

Bloch $T^{\frac{3}{2}}$ law

$$M_s(T)/M_s(0) = (1 - BT^{\frac{3}{2}}) + Ae^{-\frac{T}{T_f}} \tag{3.1}$$

which describes M_s over the complete range of temperatures. Fits to the data in figure 3.2 with equation 3.1 (shown by the solid line) results in a zero-temperature magnetization, $M_s(0) = 350 \pm 2\ emu\ cm^{-3}$. The Bloch constant was found to be $B = 2.9 \pm 0.3 \times 10^{-5}\ K^{-3/2}$. The surface spin contribution to the total $M_s(T)$ was found to be $A = 1.3 \pm 0.2 \times 10^{-3}$ and the surface spin freezing temperature $T_f = 15 \pm 1K$. With warming above $T_B \sim 20K$, the single-domain moments fluctuate about their easy axis, and with no applied field, the time-averaged magnetization is zero, and the nanoparticles are superparamagnetic. As the single-domain moments of the nanoparticles are fluctuating at a rate that is considerably greater than the measuring time, the magnetic moment of a nanoparticle may be directed at any angle with respect to an applied field direction.

For a dispersion of nanoparticles that are in thermal equilibrium with easy axis parallel to the direction of the applied field, H, the total energy per nanoparticle is described by $E = KVsin^2(\theta) - MHcos(\theta)$, where M is the particle's magnetic moment and θ is the direction the single domain makes with respect to the direction of H. Using the uniaxial anisotropy description of the energy barrier that the nanoparticle magnetization must overcome to flip orientations as described above, the temperature dependence of the coercivity is found to follow the prescription (see section 2.5)

$$H_c(T) = \frac{2K}{M_s}(1 - \sqrt{\frac{T}{T_B}}) \tag{3.2}$$

where, usually, good agreement is found with experiment based on temperature-independent K and M_s. It was postulated that for temperatures below T_B the surface anisotropy, $K_{surface}$, is providing the energy barrier for nanoparticle magnetization reversal of the total particle magnetization M_s. Figure 3.3 shows the temperature dependence of the coercivity and exchange bias for the $7nm$ particles. The solid curve is a fit using equation 3.2 with K equal to the effective surface anisotropy con-

stant determined by fitting the field and temperature dependence of the saturation magnetization.

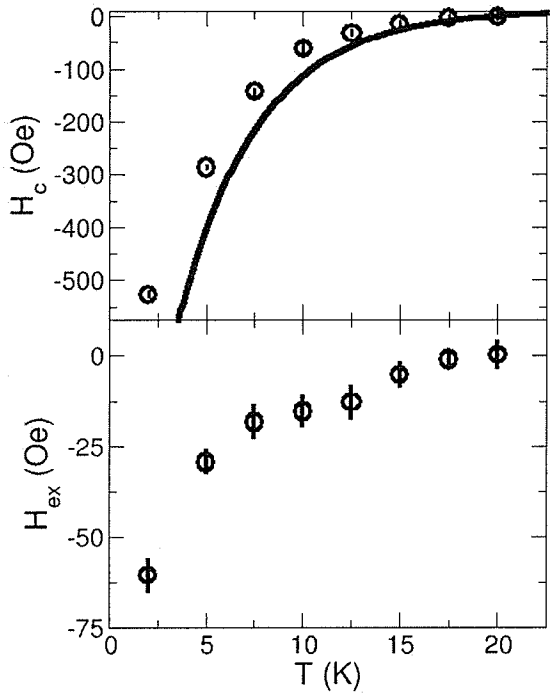

Figure 3.3: Coercivity and exchange bias

3.2 Model

In order to study the magnetic properties of maghemite nanoparticles, we shall use the following Hamiltonian

$$H = -\sum_{i<j} J_{ij}\vec{S}_i \cdot \vec{S}_j - K_s \sum_{i\in s}(\vec{S}_i \cdot \hat{n}_i)^2 - K_c \sum_{i\in c} {S_{iz}}^2 - H_z \sum_i S_{iz} \qquad (3.3)$$

where the first term describes the exchange interactions with the nearest magnetic neighbours of each site, the second term describes the single-ion uniaxial surface anisotropy, the third term accounts for the uniaxial core anisotropy and the last term is an applied magnetic field. The unit vector $\hat{n}_i$ is the local normal to the

surface of the particle. In the spinel structure the tetrahedral sites have 12 nearest neighbours on the octrahedral sites and 4 nearest neighbours on tetrahedral sites whereas the octrahedral sites have 6 nearest neighbours of each type. The corresponding superexchange interactions were taken to be antiferromagnetic with the values $J_{TT} = -42.0K, J_{TO} = -56.2K$, and $J_{OO} = -17.2K$. The surface-core exchange interactions are all divided by factor of 2 and the surface-surface interactions are divided by a factor of 10. The single-ion site surface anisotropy K_s was given the values $1.0, 5.0$ and 10.0 ,while the core anisotropy $K_c = 0.02$. These values were taken from the literature for bulk maghemite[27, 28, 29]. The spins at each site are taken to be classical spins of unit magnitude and vacancies on the octrahedral sites are given a spin magnitude of zero. The oxygen ions are considered to be non-magnetic and only serve to provide superexchange interactions between the iron sites. The actual spin of each iron atom is $S = \frac{5}{2}$ and is large enough to be treated classically at finite temperatures. However, important quantum effects are present at extremely low temperatures and we will discuss these effects later.

We take the maghemite particles to have a spherical geometry with a diameter of L unit cells as shown in figure 3.4.

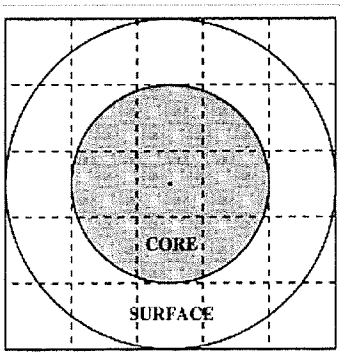

Figure 3.4: Geometry of nanoparticles

The Fe^{3+} ions in the outermost cells are called surface sites and the ions in shaded

cells are core sites. For $L = 5$ the diameter is about 4.2 nm and the particle contains 1112 surface sites, 311 core sites and 170 vacancies. For this size of particle, the majority of sites are on the surface.

Table 3.1: Number of Surface, Core and Vacant Sites

L	$Diameter(nm)$	$Surface\ Sites$	$Core\ Sites$	$Total\ Sites$	$Vacancies$
4	3.3	667	94	761	80
5	4.2	1112	311	1423	170
6	5.0	1683	751	2434	297
7	5.8	2467	1411	3878	473
8	6.6	3358	2440	5798	687
9	7.5	4327	3891	8218	971

We study particles with sizes ranging from $L = 4$ to $L = 9$ (3 to 8 nm diameter). The number of surface, core and vacant sites for $L = 4$ to 9 are given in table 3.1. The vacancies are distributed uniformly throughout the octahedral sites in both the core and surface and account for approximately 1/9 of the total sites. From table 3.1

Table 3.2: Predicted Core, Surface and Total Magnetizations

L	m_{core}	$m_{surface}$	m_{total}
4	.255	.262	.261
5	.209	.277	.262
6	.252	.247	.248
7	.256	.275	.268
8	.250	.265	.259
9	.271	.241	.255

we see that the majority of the sites are on the surface . For a perfect ferrimagnetic

order where the occupied tetrahedral sites have their spins anti-parallel to those on the octrahedral sites, we can use the data in table 3.1 to predict the values of the core, surface and total magnetization per core, surface and total number of sites as shown in table 3.2.

In our model the exchange interactions between the core, surface and core-surface sites are different. The surface and core anisotropies are also different. The exchange interactions of the surface sites differs from that of the core sites because of the symmetry breaking and surface anisotropy at the surface resulting in the unequal distribution of the magnetization.

We will use Monte Carlo techniques to study the magnetic properties of these nanoparticles. There have been many previous theoretical studies of the magnetic properties of nanoparticles. The group of Restrepo et. al. [30, 31, 32, 33] have used the Metropolis algorithm [34] to study the effect of surface anisotropy on the sublattice magnetizations with uniform exchange interactions throughout the particles. Trohidou et. al. [35, 36, 37] have also used the Metropolis algorithm to study nanoparticles with a ferromagnetic core surrounded by an antiferromagnetic surface layer. Iglesias et. al. [38, 39, 40, 41] have studied both systems with a ferromagnetic core surrounded by an anti-ferromagnetic surface layer as well as a more realistic model of maghemite with the inverse spinel structure. Several other groups [42, 43, 44, 45, 46, 47] have also used the conventional Metropolis algorithm to study the effects of surface anisotropy on the magnetic properties of maghemite nanoparticles.

The following chapter gives an overview of Monte Carlo methods and describes a different method than that used by previous studies.

Chapter 4

MONTE CARLO METHODS

4.1 Introduction

In this chapter we summarize some of the basic ideas of Monte Carlo simulations[48, 49, 50, 51]. Monte Carlo methods are used when simulating physical and mathematical systems and they were designed to provide a means to estimate answers to analytically intractable problems. The Monte Carlo method is one of the major numerical techniques developed and is widely use in all areas of science. The Monte Carlo simulation techniques apply random numbers for modeling stochastic processes in contrast to molecular dynamics techniques which use deterministic laws (e.g. Newton's equations). Monte Carlo techniques can be classified into simple sampling and importance sampling methods. When uniformly distributed random numbers are applied we have what is called the simple sampling method. Importance sampling takes advantage of weighted random numbers by means of the generation of Markov chains. The Metropolis, heat bath, and cluster algorithms are versions of the importance sampling method that have been developed in recent years.

4.2 Simple Sampling and Importance Sampling

One of the major numerical techniques which is used for evaluating integrals is the simple Monte Carlo method. We shall describe this method as applied to one-dimensional integrals. The acceptance-rejection algorithm is an example of a simple sampling technique to calculate integrals. We wish to obtain the integral of $g(x)$ over some fixed

interval,

$$I = \int_a^b g(x)\,\mathrm{d}x \tag{4.1}$$

This method corresponds to drawing a rectangular box which extends from $x = a$ to $x = b$ and from $y = 0$ to $y = y_0$ where $y_0 > g(x)$ throughout this interval. We then choose N points x, y in the box randomly using a uniform random number generator and count the number of points N_0 for which $y \leq g(x)$. This is a hit and miss algorithm and an estimate of the integral is the fraction of hits times the area of the box

$$I_e = \frac{N_0}{N}[y_0(b-a)]. \tag{4.2}$$

Another approach that can be used is to choose N values of x randomly and then evaluate $g(x)$ at each value with an estimate for the integral given by

$$I_e = \frac{1}{N}\sum_{i=1} g(x_i) \tag{4.3}$$

In this approach, as the number of values of x_i increases, the estimated result eventually converges to the correct result. However, this can require a large number of trials if the integrand $g(x)$ is not smooth. Importance sampling can be used to reduce the statistical error by choosing a weight function $w(x)$ which gives a new probability of choosing a value of x and is chosen to make $g(x)/w(x)$ a smooth function. The integral can be written as

$$I = \int_a^b g(x)\,\mathrm{d}x = \int_a^b \frac{g(x)}{w(x)}\,w(x)\mathrm{d}x = \sum_{i=1}^{n} \frac{g(x_i)}{w(x_i)} \tag{4.4}$$

where x is now chosen according to a non-uniform probability distribution $w(x)$. Non-uniform distributions can be constructed using uniform random number generators. As an example, suppose we want to generate the normalized exponential distribution

$$\begin{aligned} w(x) &= \frac{1}{\lambda}e^{-\frac{x}{\lambda}} \quad [0,\infty] \\ &= 0 \quad x < 0 \end{aligned} \tag{4.5}$$

We first calculate the integrated probability $W(x) = \int_0^x w(x')\mathrm{d}x' = 1 - e^{-\frac{x}{\lambda}}$ which satisfies $0 \leq W(x) \leq 1$ and then set it equal to a random number r chosen uniformly from the interval $[0, 1]$. Solving for x, we have $x = \lambda \ln(1-r)$ and x will be distributed according to an exponential distribution. Other non-uniform distributions can be obtained in a similar manner provided the integrated probability can be evaluated in closed form. Otherwise, a numerical procedure can be implemented.

4.3 Canonical Ensemble

The Monte Carlo method can also be used in statistical mechanics to calculate averages of various observables. The correponding integral is a multi-dimenional integral over all possible configurations of a system. Simple sampling will not work in this case. However, importance sampling can be used to choose the configurations according to the Boltzmann probability $P_i = e^{-\beta E_i}/Z$ where E_i is the total energy of the configuration, $\beta = 1/k_B T$, and Z is the canonical partition function which is a normalization factor $Z = \sum_i \exp(-\beta E_i)$. The objective of the Monte Carlo simulation is the computation of the expectation value $< A >$ of some observable A,

$$< A >= \frac{\sum_i A_i \exp(-\beta E_i)}{\sum_i \exp(-\beta E_i)} \tag{4.6}$$

If the configurations are sampled according to P_i, then the average value of A can be calculated from

$$< A >= \lim_{N \to \infty} \frac{1}{N} \sum_i A_i \tag{4.7}$$

In our case the observables of interest are the surface and core magnetizations as a function of temperature, T, and field, H.

4.4 Markov Processes

This is a stochastic process in which a sequence of configurations or states are generated. When the system is in a state i, the next state is selected with a transition

probability $M_{j\leftarrow i}$ that does not depend on the previous history of the system. Each of the transition probabilities is non-negative and not greater than unity and satisfy

$$\sum_j M_{j\leftarrow i} = 1 \tag{4.8}$$

Repeated selection of states leads to a steady-state probability distribution P_j which is an eigenvector with eigenvalue 1 of the transition matrix,

$$P_j = \sum_i M_{j\leftarrow i} P_i \tag{4.9}$$

A sufficient but not necessary condition for determining the P_i is that the transition probabilities satisfy detailed balance

$$M_{j\leftarrow m} P_m = M_{m\leftarrow j} P_j \tag{4.10}$$

which when substituted into (4.9) yields a stationary probability distribution $P_j = \sum_i M_{j\leftarrow i} P_i = \sum_i M_{i\leftarrow j} P_j = P_j$ corresponding to equilibrium.

Consider a system of spins $\vec{S}_\alpha$ in a state i, and choose a site α randomly. Now perform a virtual change in orientation of the spin at site α to create a state j. After n steps of this process, the transition probability from the initial state i to a final state f is

$$M_{f\leftarrow i}(n) = \sum_{i_1, i_2, \ldots i_{n-1}} M_{f\leftarrow i_{n-1}} M_{i_{n-1}\leftarrow i_{n-2}} \ldots M_{i_1\leftarrow i} \tag{4.11}$$

After many steps the system will approach a limiting distribution

$$P_f = \lim_{n\to\infty} M_{f\leftarrow i}(n) \tag{4.12}$$

For the canonical distribution we require the distribution to be normalized and satisfy

$$\frac{P_m}{P_j} = exp[-\beta\{E_m - E_j\}] \tag{4.13}$$

for all states m, j and, if the transition probabilities also satisfy detailed balance, then we have

$$\frac{M_{m\leftarrow j}}{M_{j\leftarrow m}} = \frac{P_m}{P_j} = exp[-\beta\{E_m - E_j\}] \tag{4.14}$$

In summary, a Markov process is a stochastic process with no memory and a full specification of the process is given by a matrix of transition probabilities $M_{j \leftarrow m}$. A desired probability distribution of states for a system is generated by repeatedly stepping from one state to another according to these transition probabilities which are required to satisfy detailed balance. There are many different choices for the transition probabilities and the Metropolis algorithm is one such choice which is widely used in Monte Carlo simulations.

4.5 The Simple Spin-Flip or Metropolis Method

The Metropolis Method[34] is the simplest and most frequently used method in the study of spin systems. The key steps of the Metropolis Algorithm are,

0. Initialize the system.

1. Choose a lattice site i at random.

2. Calculate the change in energy ΔE associated with a possible random change in the spin direction at this site.

3. Generate a random number r such that $0 < r < 1$

4. if $r < \exp(-\frac{\Delta E}{k_B T})$, accept the new spin direction. Otherwise reject it.

5. Repeat steps 1 to 4 until N spins have been either updated or not, to complete one Monte Carlo Step (mcs).

6. Repeats steps 1 to 5 until sufficient data is collected.

One Monte Carlo Step (MCS) corresponds to updating all the spins in the system. This approach is simple to implement but can lead to a large number of rejected updates if the changes in the spin directions are chosen randomly.

4.6 The Heat Bath Method

The heat bath Monte Carlo method[52, 53] generates a sequence of configurations which simulate a canonical ensemble of states in thermal equilibrium at a constant temperature T. Given a configuration of the spins in a system, the direction of each spin is updated assuming that the spin is in contact with a heat bath that puts it into local equilibrium with the surrounding spins. For systems that are described by a Hamiltonian of the form

$$H = -\sum_{<ij>} J_{ij}\vec{S}_i \cdot \vec{S}_j \tag{4.15}$$

where $\vec{S}_i$ is a classical vector with 3 components located at the site i of a lattice and J_{ij} is the strength of the exchange interaction between nearest neighbour pairs of spins, the orientation of the spin $\vec{S}_i$ is determined by the net effect of the neighbouring spin orientations, the strength of the interaction J_{ij} and the temperature T. The neigbouring spins exert a local effective magnetic field at site i given by

$$\vec{H}_i^{eff} = \sum_j J_{ij}\vec{S}_j \tag{4.16}$$

This field direction provides a local coordinate frame for the spin $\vec{S}_i$. In the case of classical spins, the spin direction with respect to the local field $\vec{H}_i^{eff}$ can be described using the azimuthal and polar angles ϕ_i and θ_i respectively. The equilibrium probability of the spin direction at site i is given by the Boltzmann factor

$$P(\theta_i, \phi_i) = \frac{e^{\beta\vec{S}_i \cdot \vec{H}_i^{eff}}}{C} \tag{4.17}$$

where C is a normalization factor. Note that

$$\vec{S}_i \cdot \vec{H}_i^{eff} = |\vec{S}_i||\vec{H}_i^{eff}|\cos(\theta_i) = H_i^{eff}\cos(\theta_i) \tag{4.18}$$

The normalization factor C is given by the integral

$$\begin{aligned} C &= \int_0^{2\pi}\int_0^{\pi} e^{(\beta)H_i^{eff}\cos(\theta_i)}\sin(\theta_i)d\theta_i d\phi_i \\ &= 4\pi\frac{\sinh(\beta H_i^{eff})}{\beta H_i^{eff}}. \end{aligned} \tag{4.19}$$

Hence the normalized probability distribution for a classical spin can be written as

$$P(\theta_i, \phi_i) = \frac{\beta H_i^{eff} e^{\beta H_i^{eff} \cos(\theta_i)}}{4\pi \sinh(\beta H_i^{eff})} \tag{4.20}$$

We can separate this into the product of independent distributions for $\cos(\theta_i)$ and ϕ_i as follows

$$P(\phi_i) = \int_{-1}^{1} P(\cos(\theta_i), \phi_i) d\cos(\theta_i) = \frac{1}{2\pi} \tag{4.21}$$

$$\begin{aligned} P(\cos(\theta_i)) &= \int_0^{2\pi} P(\cos(\theta_i), \phi_i) d\phi_i \\ &= \frac{1}{2} \frac{\beta H_i^{eff} e^{\beta H_i^{eff} \cos(\theta_i)}}{\sinh(\beta H_i^{eff})} \end{aligned} \tag{4.22}$$

A random number generator can now be used to generate values of the independent variables $\cos(\theta_i)$ and ϕ_i which are distributed according to the probability functions $P(\cos(\theta_i))$ and $P(\phi_i)$. The integrated probability distributions are in the range [0,1] and can be set equal to a random number which is uniformly distributed on this same interval. In general, for a variable x which has a probability density $P(x)$, the

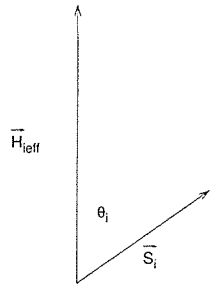

Figure 4.1: At each site i there is an instantaneous local field $\vec{H}_i^{eff} = \sum_j J_{ij} \vec{S}_j$. The azimuthal angle ϕ_i singles out a plane containing both $\vec{H}_i^{eff}$ and $\vec{S}_i$. The orientation of $\vec{S}_i$ with respect to $\vec{H}_i^{eff}$ in this plane is described by the polar angle θ_i.

cumulative probability distribution

$$P_c(X) = \int_{-\infty}^{X} P(x)dx \tag{4.23}$$

represents the probability of choosing a value of the variable x to be less than or equal to X. We set $P_c(X) = r$ where r is uniformly distributed on the unit interval and solve for X in terms of r. Hence for the $\cos(\theta_i)$ and ϕ_i we can write

$$\begin{aligned} P_c(\cos(\Theta)) &= \int_{-1}^{\cos(\Theta)} P(\cos(\theta_i))d\cos(\theta_i) = r1 \\ P_c(\Phi) &= \int_{0}^{\Phi} P(\phi_i)d\phi_i = r2 \end{aligned} \tag{4.24}$$

where $r1, r2$ are independent random numbers uniformly distributed on $[0, 1]$. Equations (4.24) can be inverted to yield

$$\begin{aligned} \cos(\Theta) &= 1 + \frac{1}{\beta H_i^{eff}} \ln\left((1 - r1)e^{-2\beta H_i^{eff}} + r1\right) \\ \Phi &= 2\pi r2 \end{aligned} \tag{4.25}$$

The random numbers $r1, r2$ are generated and the new direction of the spin relative to the local field direction is chosen using the above method. Since the local field direction is known, this new spin direction can then be transformed from the local frame defined by $\vec{H}_i^{eff}$ to the global coordinate system. This heat bath method generates spin updates which are in agreement with the Boltzmann canonical probability distribution and consequently the principle of detailed balance is always satisfied. At each Monte Carlo step, there is a spin update and hence no moves are rejected. This is a very efficient way to sample the accessible microstates.

When the Hamiltonian also includes anisotropies such as in (3.3), we can still define an effective magnetic field as follows

$$\vec{H}_i^{eff} = -\partial H/\partial \vec{S}_i = \sum_j J_{ij}\vec{S}_j + 2K_s(\vec{S}_i.\hat{n}_i)\hat{n}_i\delta_{i,s} + 2K_c S_{iz}\hat{k}\delta_{i,c} + H_z\hat{k} \tag{4.26}$$

4.7 *Semi-classical Method*

It is well known that classical physics fails to describe the correct thermodynamic behaviour of systems at low temperatures. For example, if we consider a single classical spin in the presence of a field H at temperature T, the average component of the spin in the direction of the field is given by the Langevin function $L(H/T) = coth(H/T) - T/H$ which approaches unity linearly with T as $T \rightarrow 0$. However, a quantum spin of magnitude $\sqrt{S(S+1)}$ can only have a discrete number of components along the field direction. The approach to the maximum allowed component along the field direction is exponential in T in this case. As shown below, a semi-classical picture of the possible spin orientations in a field is a set of cones with the field along the cone axis

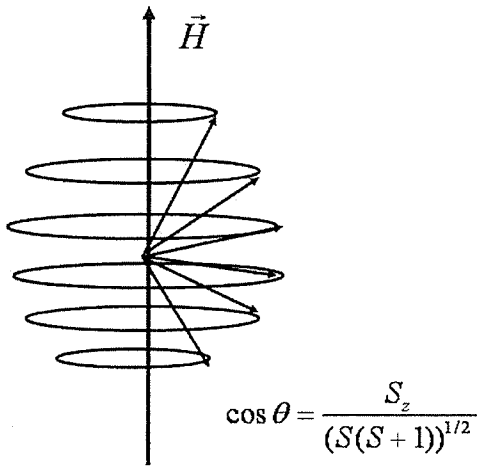

Figure 4.2: Semiclassical description of spin with $S = 5/2$

The heat bath algorithm described in the previous section allows the cone angle θ to have any value in the range $[0, \pi]$. We use the heat bath algorithm to generate a value of $cos\theta$ but we then place the spin direction relative to the effective field

onto the nearest cone. This procedure has little effect at high temperatures but does modify the low temperature dependence of the magnetization, energy and specific heat. We start the simulation at high temperature and cool in either zero or non-zero applied field. We measure the energy, specific heat, core and surface magnetizations as a function of temperature. At low temperatures we also measure hysteresis loops. Typically we use $30,000$ *mcs* for our measurements at each value of H and T. We have studied particles with sizes ranging from $L = 4$ to 9 (3 to 8 nm diameter).

Chapter 5

MONTE CARLO RESULTS

In this chapter we present the results of our Monte Carlo simulations of the magnetic properties of the model described in Chapter 3. We have calculated the core, surface and total magnetizations of the particles described in tables 3.1 and 3.2 as a function of temperature when the system is cooled in both zero and non-zero applied fields. We have considered the cases where the surface anisotropy constant has the values $K_s = 1, 5$ and 10 which represent weak, intermediate and strong anisotropy. We have also studied hysteresis loops at low temperatures for both the zero and non-zero field cooled cases.

5.1 Thermal Dependence of the Magnetization

The temperature dependence of the magnetization can give important information about the properties of the nanoparticles. In the classical model we have a unit vector at each Fe site in the nanoparticle. The core, surface and total magnetizations are given by

$$\begin{aligned} \vec{m}_{core} &= \frac{1}{n_{core}} \sum_{i \in core} \vec{S}_i \\ \vec{m}_{surf} &= \frac{1}{n_{surf}} \sum_{i \in surf} \vec{S}_i \\ \vec{m}_{tot} &= \frac{1}{n_{tot}} \sum_{i \in tot} \vec{S}_i \end{aligned} \tag{5.1}$$

where n_{core}, n_{surf} and n_{tot} are the number of occupied core, surface and total sites as given in table 3.1. We have calculated average values of each component of the magnetization as well as the magnitude squared at each temperature using the Monte

Carlo method described in the previous chapter. The particle is initialized at high temperature with the spins in random directions. The Monte Carlo updates are then performed for 1000 Monte Carlo steps (mcs) and the measurements are collected over the next 5000 mcs at this temperature. The temperature is then lowered and the process is repeated.

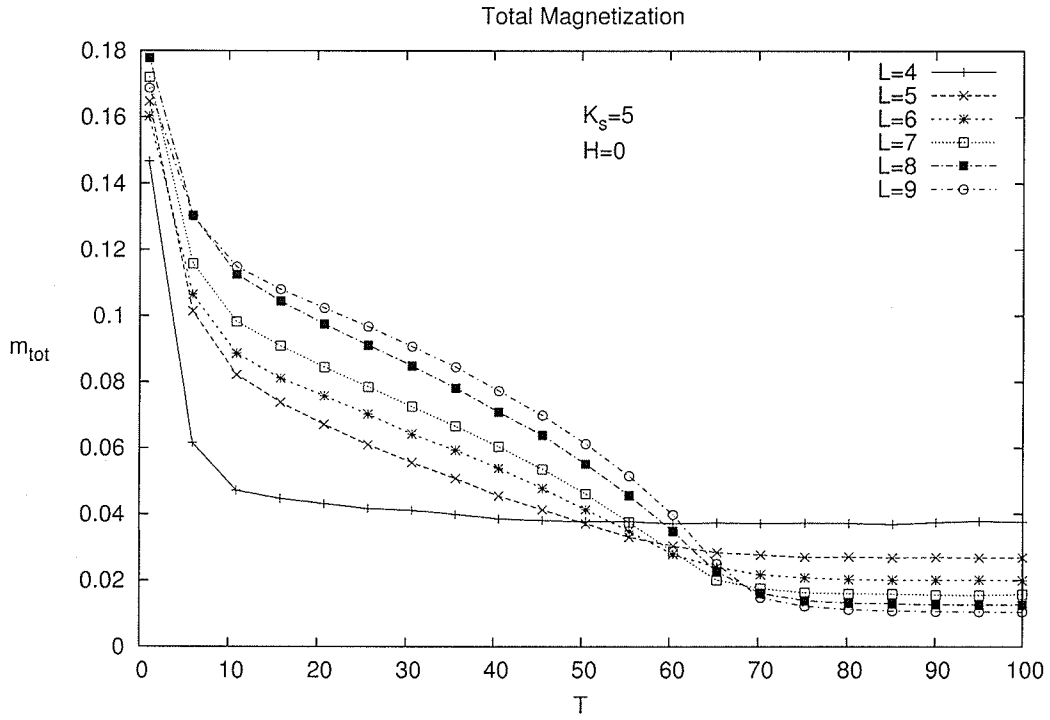

Figure 5.1: Magnitudes of the total magnetization as a function of temperature for particle sizes ranging from $L = 4$ to $L = 9$. The surface anisotropy constant has the value $K_s = 5$ and the applied field $H = 0$.

Figure 5.1 shows a plot of the magnitude of the total magnetization for particle sizes ranging from $L = 4$ to $L = 9$ as a function of T when cooled in zero applied field. The surface anisotropy constant has the value $K_s = 5$. At high T, the magnetization magnitudes do not vanish but rather approach $\frac{1}{\sqrt{n_{tot}}}$ with the larger values of L lying below those of smaller L. This is easily understood from the formula for the

magnetization squared

$$\begin{aligned} < m^2 > &= \frac{1}{N^2} \sum_{i,j} < \vec{S}_i . \vec{S}_j > \\ &= \frac{1}{N^2} \left[\sum_i < S_i^2 > + \sum_{i \neq j} < \vec{S}_i . \vec{S}_j > \right] = \frac{1}{N} \end{aligned} \tag{5.2}$$

where the terms with $i = j$ in the sum are unity since the spins are unit vectors and the terms with $i \neq j$ decouple and vanish at high T. At lower temperatures, these latter terms contribute and the magnetizations with smaller L lie below those of larger L. The crossover for a given pair of sizes occurs at temperatures in the range from $T = 50$ to $T = 70$. For the largest size pair, the crossover is near $T_c \sim 68$. We identify this temperature with the ordering temperature of the particle where strong correlations between neighbouring spin directions develop. This value of T_c differs from the experimental value of T_c for maghemite particles of these sizes by an order of magnitude because our model uses classical unit vectors for the Fe ions whereas the actual spin length is $J = g_J S = 5$ which would give an extra factor of $J(J+1)/3 = 10$ in the ordering temperature that has not been included in the definition of our exchange constants. Including this factor would yield an ordering temperature of the order of $680^0 K$ which does lie in the range of the experimental values. Hence our temperature scale is about a factor of 10 smaller than the experimental temperature scale. Below T_c, the total magnetization increases with decreasing temperature and displays an even more rapid increase below about $T \sim 5$.

The total magnetization includes contributions from both the core and surface sites. Although the core develops order at T_c, the surface sites can remain disordered until much lower temperatures. The Monte Carlo approach allows us to separate these two contributions. Fig. 5.2 shows the magnitudes of both the core and surface magnetizations as a function of T.

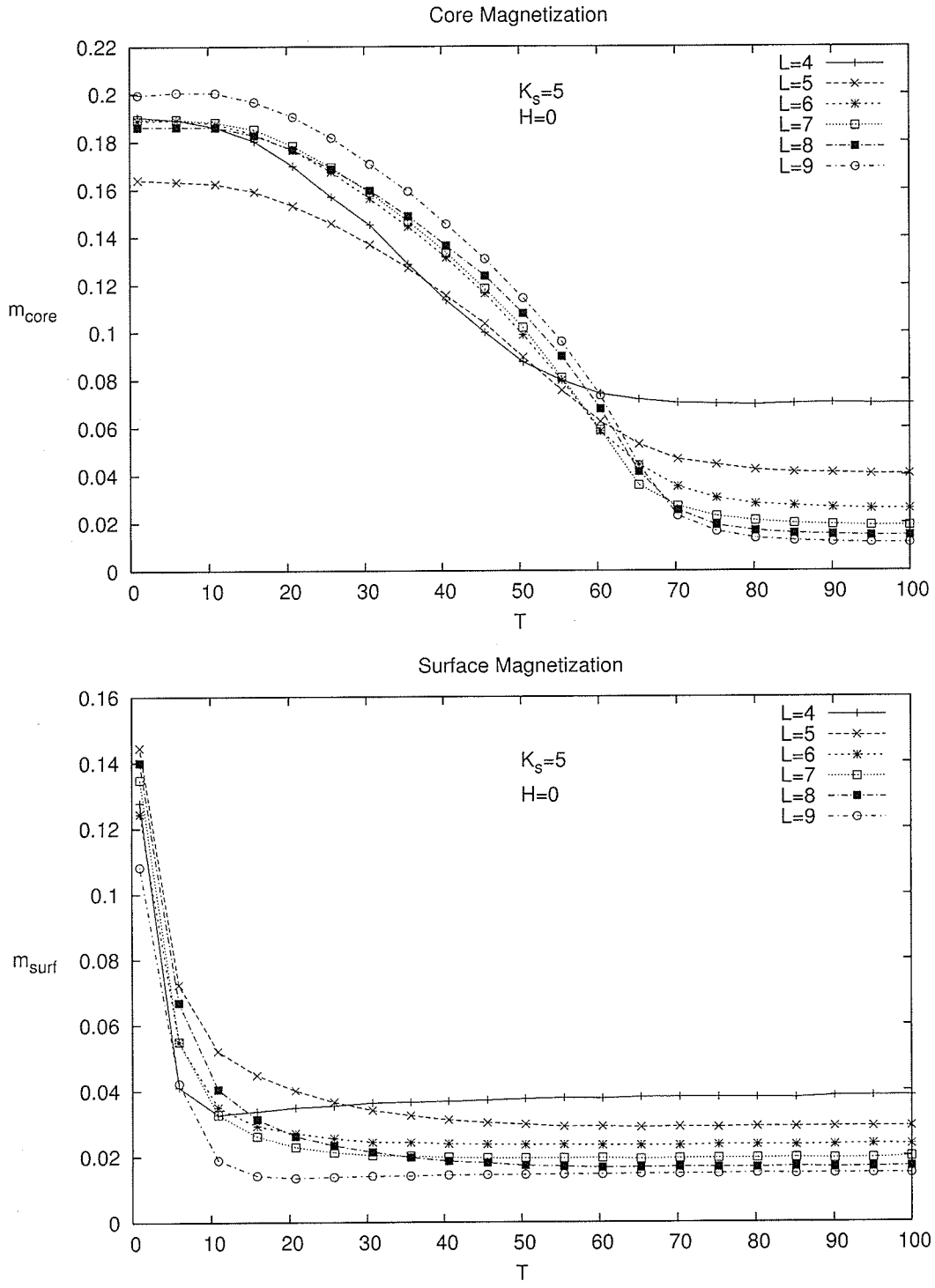

Figure 5.2: Magnitudes of the core (upper panel) and surface (lower panel) magnetizations as a function of temperature for particle sizes ranging from $L = 4$ to $L = 9$. The surface anisotropy constant has the value $K_s = 5$ and the applied field $H = 0$.

The core magnetizations begin to develop at about $T_c \sim 68$ and saturate at low T. The values of the magnetizations at $T = 0$ are slightly less than those predicted in table 3.2 for perfect ferrimagnetic order but indicate that we do have a ferrimagnetic order in the core which is not perfect. In contrast, the surface magnetizations remain zero down to very low temperatures and increase substantially only below $T \sim 5$. The particles with small L are dominated by surface sites and only have a small number of core sites. The particles have ferrimagnetic order with a small amount of disorder due to the oxygen vacancies on the octrahedral sublattice which weaken the exchange interactions. The surface sites are also affected by the reduced coordination number at the spherical surface. Note that the $T = 0$ core magnetizations are reduced much more for small L and that the surface magnetizations are reduced even more than those of the core for all sizes.

Additional information can be obtained by measuring the vector components of the total magnetization as the temperature is reduced. Fig. 5.3 shows the components and the magnitude of the total magnetization as a function of T for $L = 7$ in two temperature ranges. The upper panel indicates that all the components essentially average to zero at high T, which indicates that the particles are paramagnetic in this temperature range. The non-vanishing of the magnitude is a finite size effect as discussed previously. Below $T_c \sim 68$, the components of $\vec{m}_{tot}$ fluctuate from one temperature to another with an increasing amplitude and the magnitude increases smoothly. This indicates that the particle is developing ferrimagnetic order but it is not blocked in this range of temperature. Although the particle has a net moment, it is superparamagnetic since the direction of the net moment can overcome thermal barriers and change its direction spontaneously. At much lower temperatures (lower panel), the components of $\vec{m}_{tot}$ cease to fluctuate and become blocked below the blocking temperature $T_B \sim 3$.

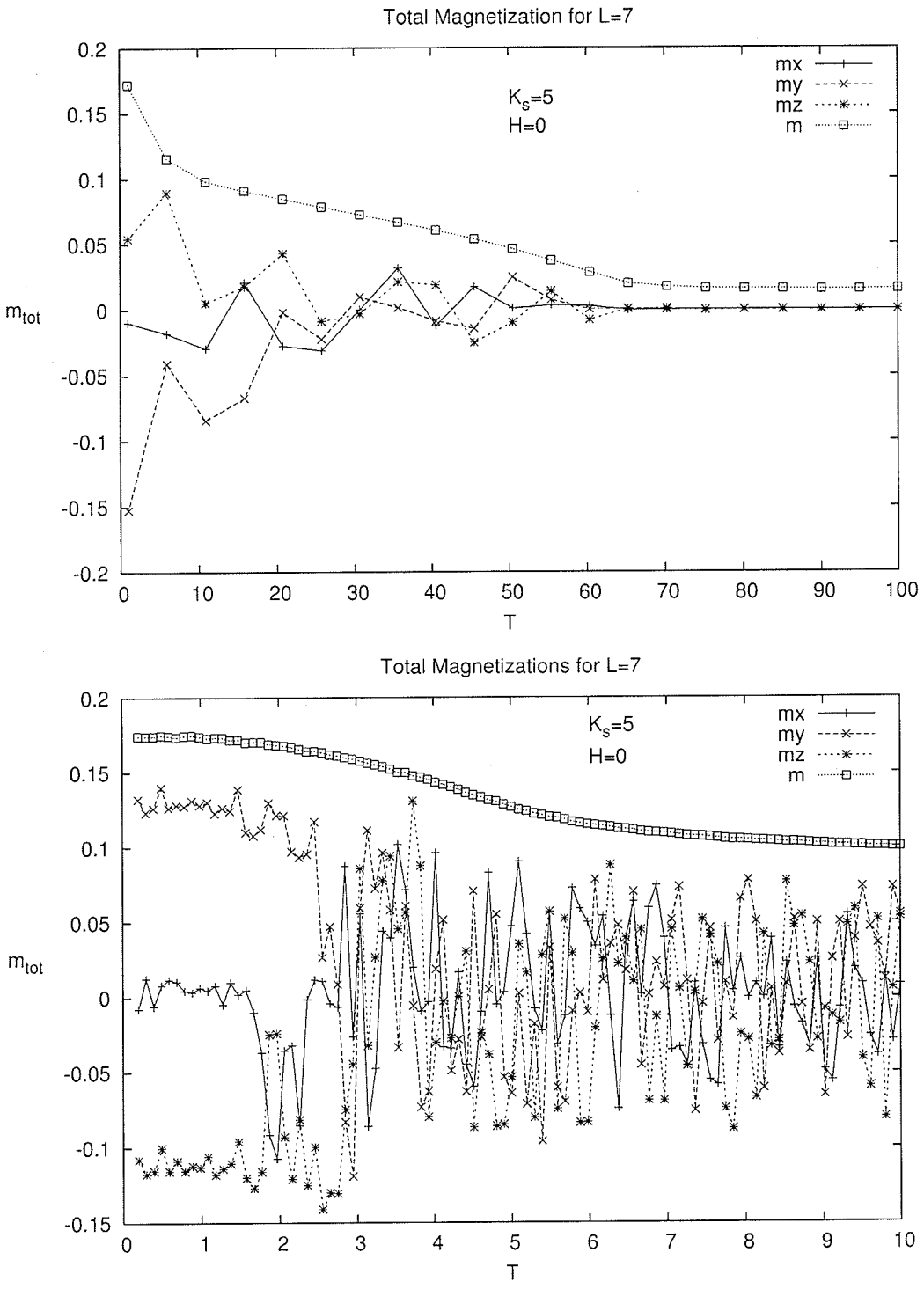

Figure 5.3: Components and magnitude of the total magnetization as a function of temperature for particle size $L = 7$ in two temperature ranges. The surface anisotropy constant has the value $K_s = 5$ and the applied field $H = 0$.

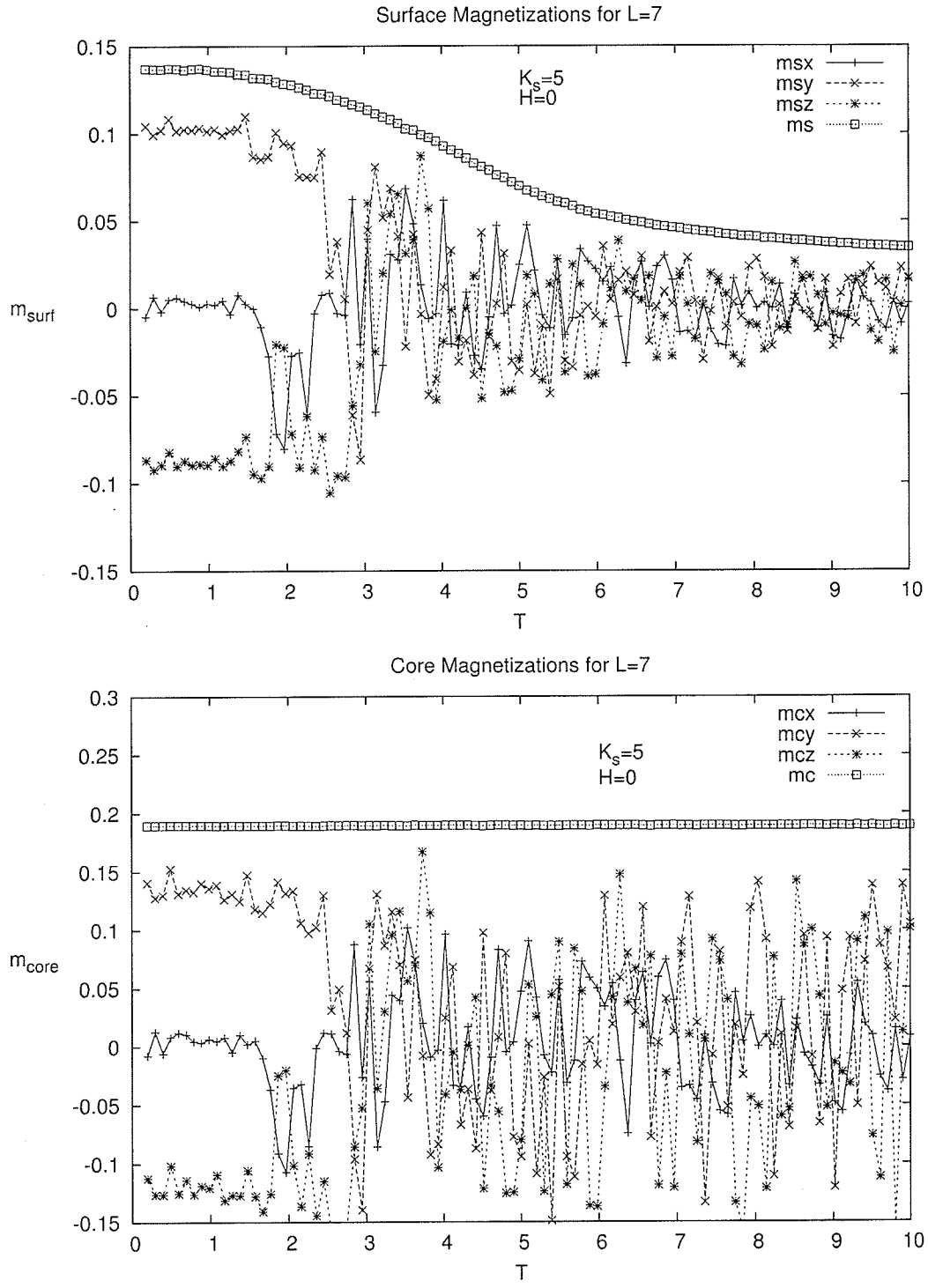

Figure 5.4: Components and magnitude of the surface (upper panel) and the core (lower panel) magnetization as a function of temperature for particle size $L = 7$. The surface anisotropy constant has the value $K_s = 5$ and the applied field $H = 0$.

Fig. 5.4 shows the components and magnitudes of the surface and core magnetizations at low T for $L = 7$. In both cases, the magnitudes vary smoothly but the components fluctuate from one temperature to another until below $T_B \sim 3$ where both the surface and core magnetizations become blocked and cannot overcome the thermal barriers. The surface magnetization appears to develop at a slightly higher temperature $T_s \sim 6$ which is about 10% of T_c. All of these results are for a value of the surface anisotropy $K_s = 5$. Similar behaviour is observed for all particle sizes.

We have repeated the calculations with a smaller values of the surface anisotropy constant. For $K_s = 1$, the surface and core magnetizations are shown in Fig. 5.5. The components of the magnetizations exhibit strong fluctuations down to much lower temperatures than for $K_s = 5$. The surface ordering temperature is reduced to $T_s \sim 3$ and the blocking temperatures are reduced to $T_B \sim 0.5$.

For larger values of the surface anisotropy, the surface ordering and blocking temperatures are increased. For $K_s = 10$, the blocking temperatures are increased to $T_B \sim 4.5$ and the surface appears to order at $T_s \sim 8$, as shown in Fig. 5.6. This behaviour is again characteristic of all particle sizes. For all values of K_s and L, the core and surface magnetizations appear to block at the same temperature but have different ordering temperatures.

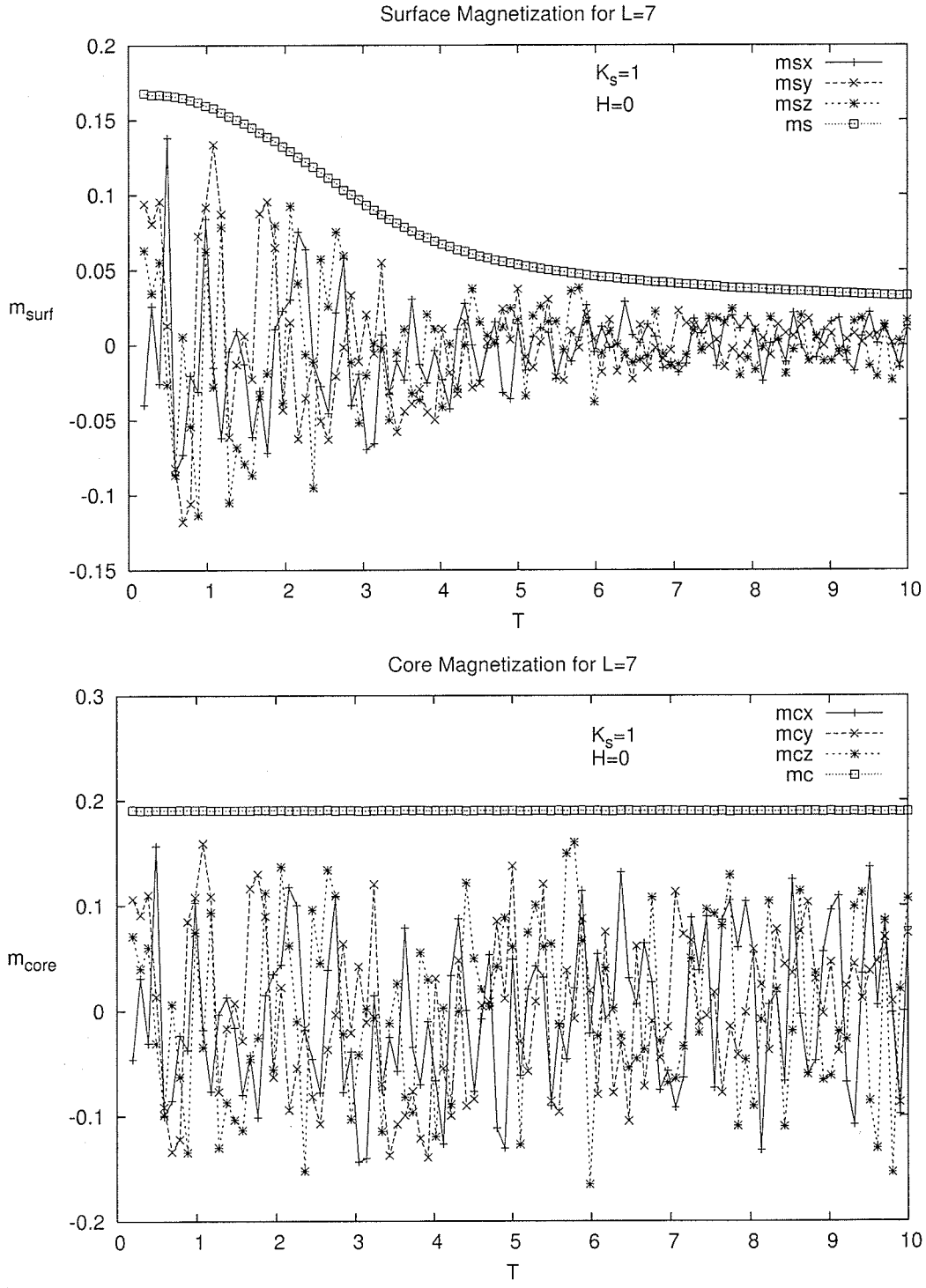

Figure 5.5: Components and magnitude of the surface (upper panel) and core (lower panel) magnetizations as a function of temperature for particle size $L = 7$. The surface anisotropy constant has the value $K_s = 1$ and the applied field $H = 0$.

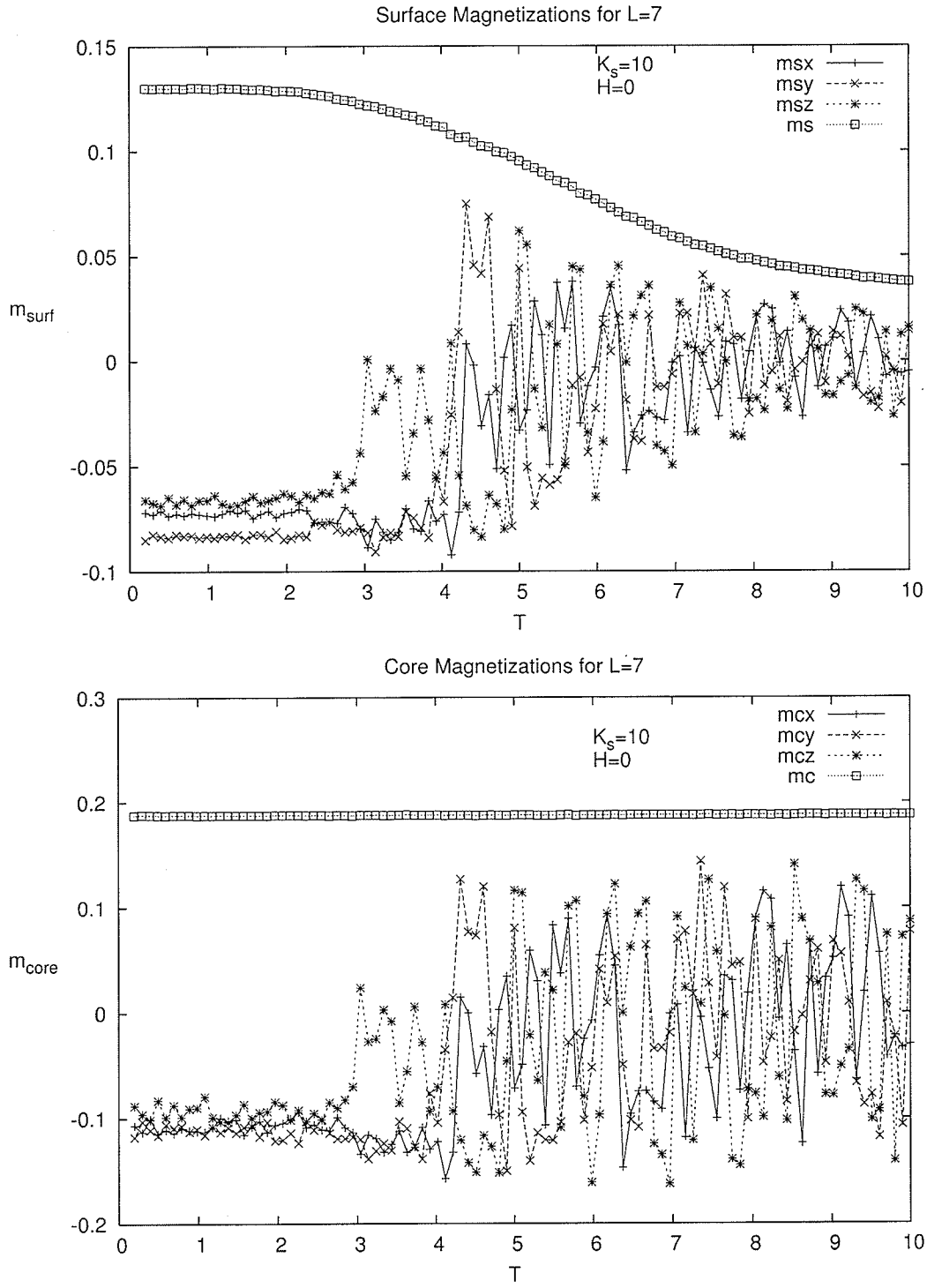

Figure 5.6: Components and magnitude of the surface (upper panel) and core (lower panel) magnetizations as a function of temperature for particle size $L = 7$. The surface anisotropy constant has the value $K_s = 10$ and the applied field $H = 0$.

The values of T_B estimated from the temperature dependence of the magnetization components are tabulated in table 5.1 for the different values of L and K_s. The blocking temperature seems to be fairly independent of L, which is a measure of the particle size, but increases with K_s.

Table 5.1: Blocking Temperature T_B for various L and K_s

L	$K_s = 1$	$K_s = 5$	$K_s = 10$
4	0.3	2.9	4.0
5	0.4	3.2	4.2
6	0.4	3.0	4.4
7	0.5	3.0	4.5
8	0.5	2.7	4.5
9	0.5	3.0	4.5

Fig. 5.7 shows a plot of T_B versus L for fixed K_s as well versus K_s for fixed L. The fact that T_B is almost independent of the size of the particle is unexpected since, for a single domain particle, T_B should be proportional to the volume of the particle. However, the blocking temperature increases approximately proportionally to K_s.

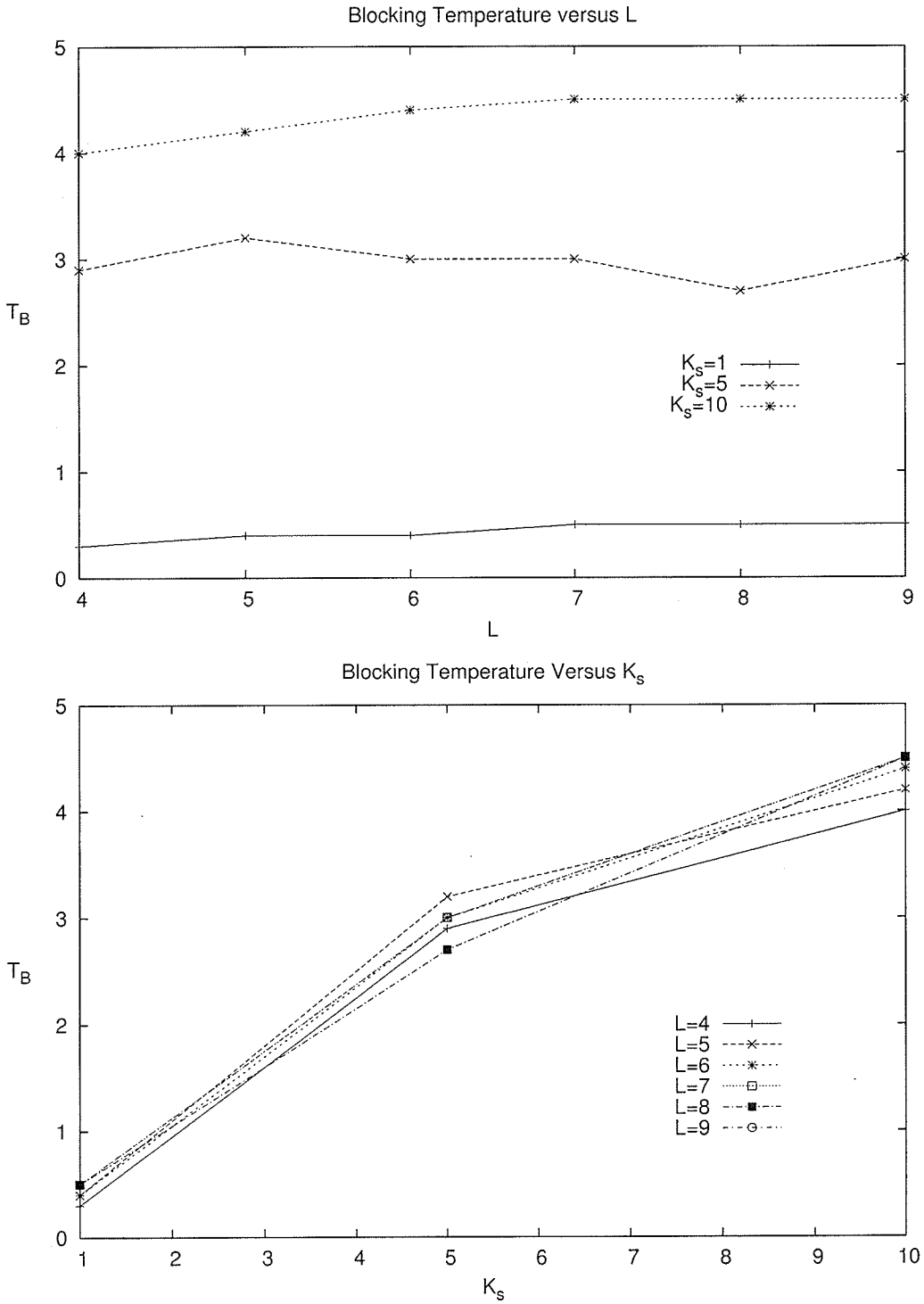

Figure 5.7: T_B versus L for surface anisotropy $K_s = 1, 5, 10$ (upper panel) and versus K_s for $L = 4, 5, 6, 7, 8, 9$ (lower panel).

The surface magnetizations for $K_s = 5$ shown in the lower panel of Fig. 5.2 can be fit to a expression of the form

$$m_{surf}(T) = a \exp(-T/T_s) + b \tag{5.3}$$

where b describes the finite size effects at high T and for each L has the value $\frac{1}{\sqrt{n_{surf}}}$. This form is the same as that used to fit the experimental data described in chapter 3. The fits were carried out over the temperature range $[1, 50]$ and the fitting parameters are tabulated in table 5.2. The values of T_s are slightly larger than the values of T_B determined from the components of the magnetization and indicate the temperature where the surface spins develop order but are not yet blocked.

Table 5.2: Fit to $m_{surf}(T) = ae^{-T/T_s} + b$ for $K_s = 5$.

L	a	b	T_s
4	0.13 ± 0.01	0.034 ± 0.094	2.91 ± 0.39
5	0.13 ± 0.01	0.033 ± 0.001	5.83 ± 0.40
6	0.13 ± 0.01	0.024 ± 0.001	4.75 ± 0.35
7	0.15 ± 0.01	0.020 ± 0.001	4.69 ± 0.32
8	0.15 ± 0.01	0.019 ± 0.001	5.93 ± 0.35
9	0.13 ± 0.01	0.013 ± 0.001	4.29 ± 0.36

However, if we increase the number of temperature points in the range $[0.2, 10]$ as shown in Figs. 5.4 - 5.6, then the exponential form is not appropriate. The modified form

$$m_{surf}(T) = a \exp(-(T/T_s)^n) + b \tag{5.4}$$

works extremely well. Table 5.3 shows the values of T_s and the exponent n for $K_s = 1, 5$ and 10. The value of T_s increases with K_s in much the same way as T_B but is fairly independent of L. T_s is larger than T_B which seems to indicate that

the surface develops order before the particle becomes blocked as the temperature is reduced. The exponent n is also independent of L but increases with the value of K_s.

Table 5.3: Fit to $m_{surf}(T) = ae^{-(\frac{T}{T_s})^n} + b$ for $K_s = 1,\ 5$ and 10

	$K_s = 1$		$K_s = 5$		$K_s = 10$	
L	T_s	n	T_s	n	T_s	n
4	2.92 ± 0.01	2.30 ± 0.02	4.40 ± 0.01	3.02 ± 0.04	5.99 ± 0.02	3.75 ± 0.05
5	3.25 ± 0.03	1.84 ± 0.04	4.82 ± 0.03	2.60 ± 0.05	6.19 ± 0.03	3.32 ± 0.05
6	3.38 ± 0.02	1.96 ± 0.04	4.99 ± 0.02	2.86 ± 0.04	6.34 ± 0.02	3.72 ± 0.04
7	3.34 ± 0.02	1.88 ± 0.03	4.88 ± 0.02	2.64 ± 0.03	6.24 ± 0.01	3.27 ± 0.02
8	3.64 ± 0.02	1.81 ± 0.03	5.19 ± 0.02	2.54 ± 0.03	6.57 ± 0.01	3.19 ± 0.02
9	3.59 ± 0.02	1.92 ± 0.03	5.15 ± 0.01	2.69 ± 0.02	6.54 ± 0.01	3.27 ± 0.02

Fig. 5.8 shows plots of the surface ordering temperature T_s as a function of L (upper panel) and K_s (lower panel). The behaviour can be compared to that of the blocking temperature T_B in Fig. 5.7. Both T_B and T_s display the same qualitative behaviour with $T_s > T_B$ as a function of L and K_s. This suggests that the particle blocking is associated with the surface ordering and that the surface anisotropy plays an important role in both quantities.

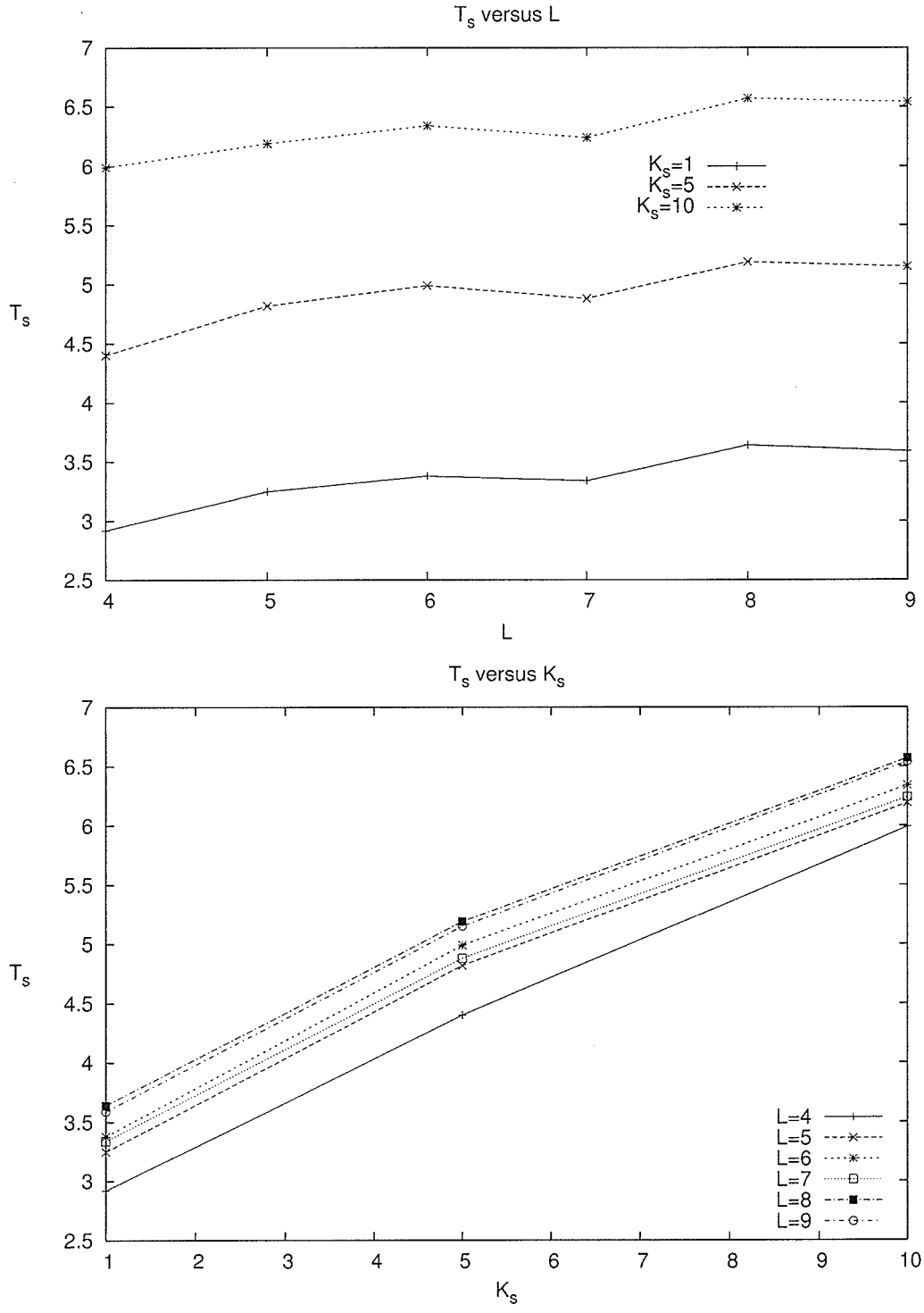

Figure 5.8: T_s versus L for $K_s = 1, 5, 10$ (upper panel) and T_s versus K_s for $L = 4, 5, 6, 7, 8, 9$ (lower panel).

5.2 *Field Cooling*

We have also studied the magnetic properties of the nanoparticles when they are cooled in the presence of a non-zero field. The field cooling procedure starts from a random spin configuration at high T and then the temperature is slowly reduced to $T = 1$. During the cooling, we measure the total, core and surface magnetizations. Fig. 5.9 shows the magnetizations for both the zero field and non-zero field cases with $L = 7$ and $K_s = 5$. The lower panel of the figure shows that the magnetizations are increased in the field cooled case. At the lowest temperature, the surface magnetization has almost doubled compared to the zero field case. The magnitude of the applied field is the same as the magnitude of the surface anisotropy and these contributions to the energy of the particle are in competition.

The surface anisotropy favours the surface moments to be normal to the surface whereas the applied field favours alignment in a particular direction. When cooled in zero field, the surface anisotropy leads to some of the surface moments pointing outward from the surface and some inward as both satisfy the normal arrangement. Hence the surface anisotropy can lead to a net moment reduction. In the presence of a field, the direction of the surface moments will change and will point outward or inward according to whether the outward normal has a component parallel or anti-parallel to the field. The net effect is an increase in the net surface moment as shown schematically in Fig. 5.10.

We can examine the spin configurations in detail at the lowest temperature using the Monte Carlo method. Fig. 5.11 shows the ground state surface configurations for $L = 4$ and $K_s = 5$ in the two cases. Careful examination shows that there is an increased polarization of the moment after cooling in a non-zero field.

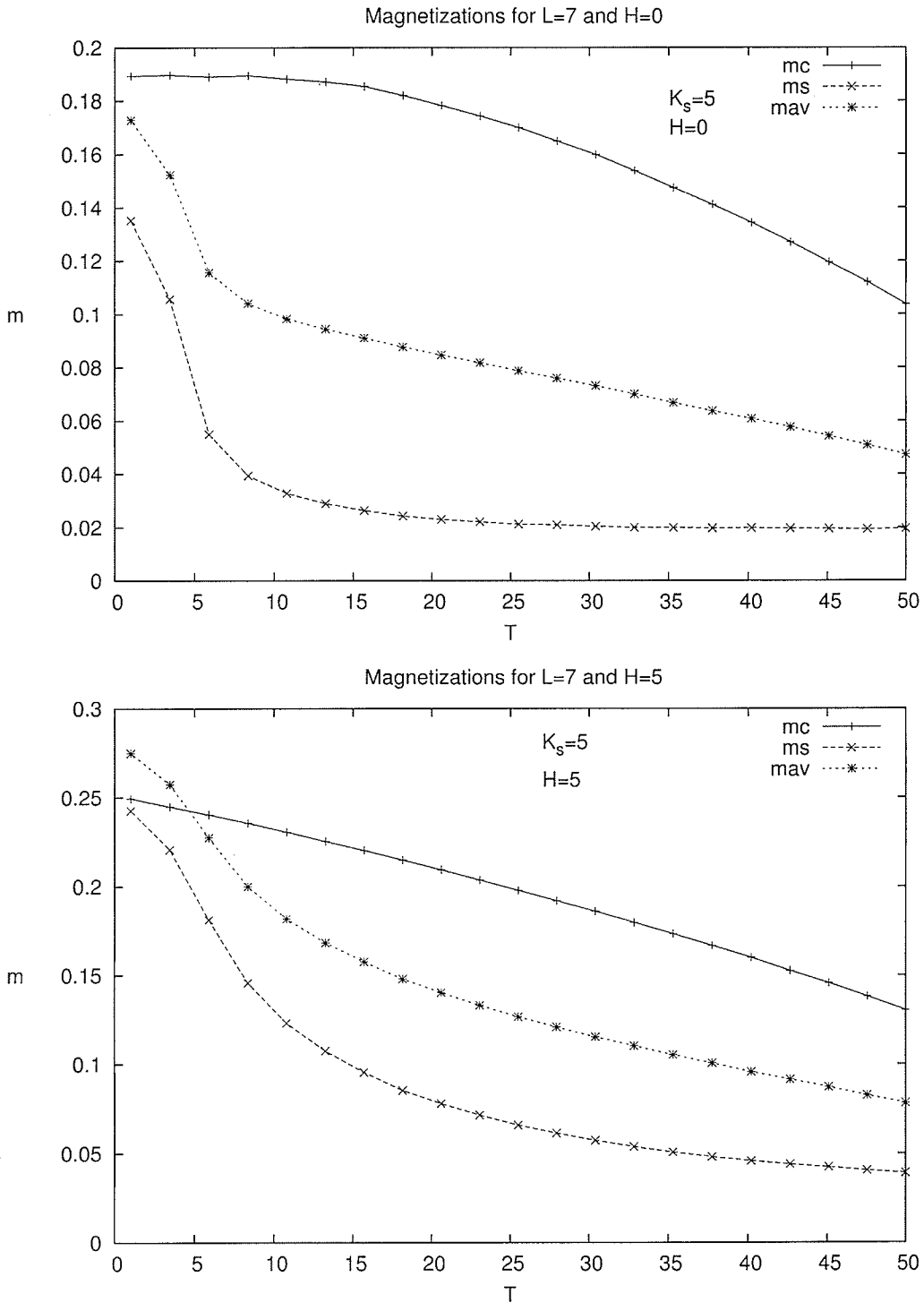

Figure 5.9: Magnitudes of the total, core and surface magnetizations as a function of temperature for particle size $L = 7$ when cooled in a field of magnitude $H = 0$ (upper panel) and a field $H = 5$ (lower panel). The surface anisotropy constant has the value $K_s = 5$ in both cases.

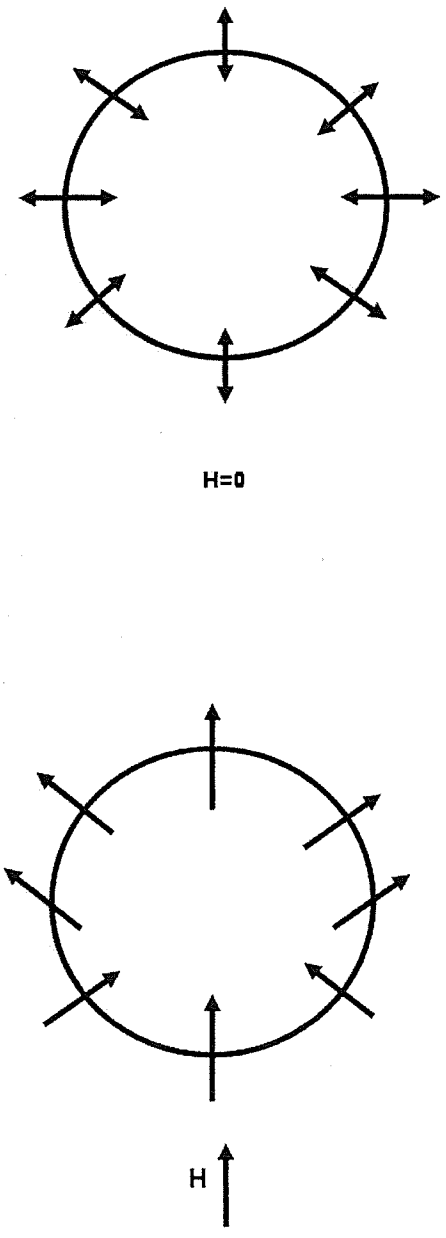

Figure 5.10: Zero-field cooled and non-zero field cooled configurations

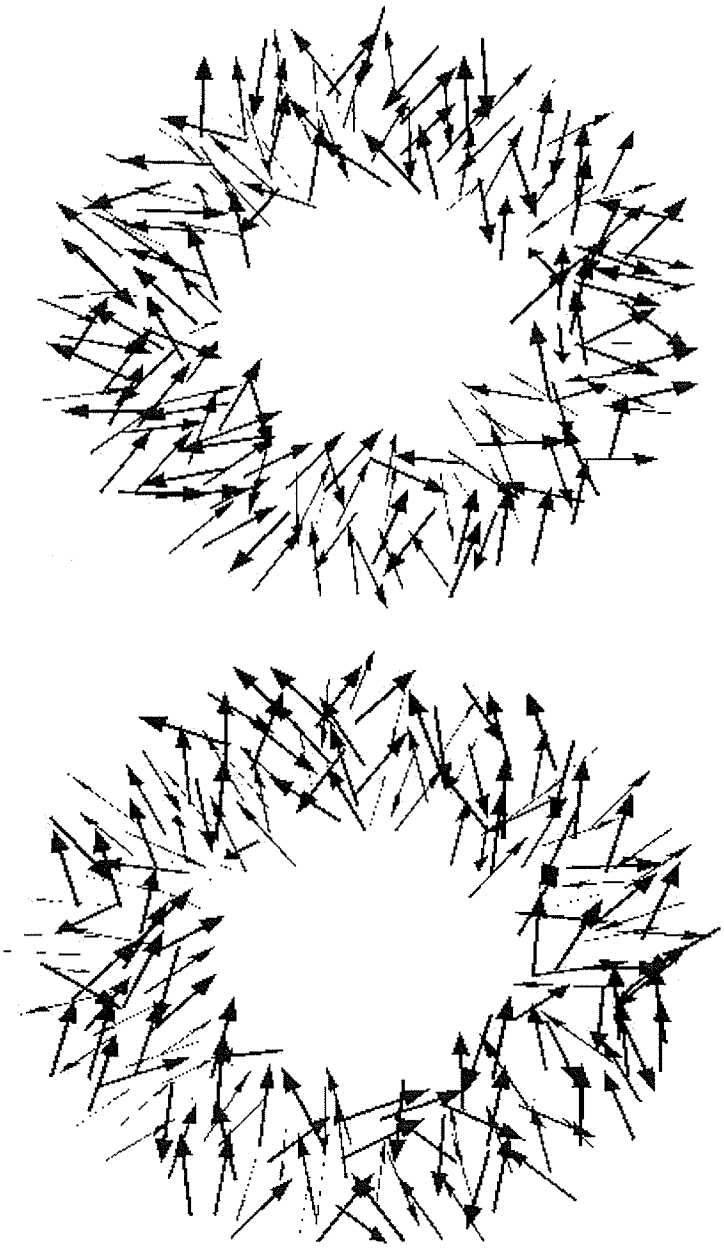

Figure 5.11: Zero-field cooled (upper panel) and non-zero field cooled (lower panel) ground state configurations for $L = 4$ and $K_s = 5$

5.3 *Hysteresis Loops*

After cooling the particle in either zero field or non-zero field, we have measured the hysteresis properties of a nanoparticle. In each case we begin at the lowest temperature with a field applied in the z-direction and slowly reduce its magnitude to zero and then slowly increase the field in the reversed direction until the magnitude is the same as it was at the beginning. This process is then carried out in the reverse direction. At each value of the applied field, we perform 30,000 mcs to measure the components of the magnetization and the energy. Magnetic contributions to the total magnetization per site arising from the surface and core sites were computed separately.

Fig. 5.12 shows typical hysteresis loops for $L = 7$ and $K_s = 5$ for the zero-field cooled case at various temperatures. The upper panel corresponds to the range $1 < T < 5$ and indicates that the width of the hysteresis loop quickly narrows as the blocking temperature is reached. T_B was estimated to be approximately 3.0 for this size of particle. The lower panel shows hysteresis loops in the narrower range $1 < T < 1.4$. As the applied field is reduced in magnitude and reversed, the component of the magnetization in the z-direction slowly decreases until it rapidly changes direction near $H_z \sim -0.2$. However, the reversal is not complete until $H_z \sim -0.4$. Similar behaviour is observed along the return path as H_z is increased to positive values. At the lowest temperature $T = 1$, the coercive field (as measured by when the magnetization changes sign) is $H_c \sim 0.25$. The $T = 1$ loop appears to have sub-loops when the magnitude of the applied field is between 0.2 and 0.4 which indicate that complete reversal does not occur immediately.

Fig. 5.13 shows the energy per particle as a function of the applied field (upper panel) and all three components of the total magnetization versus field (lower panel). As the field is reduced from $H_z = 0.6$, the energy increases reaching a maximum near $H_z \sim -0.2$ and drops abruptly as the field is reduced further.

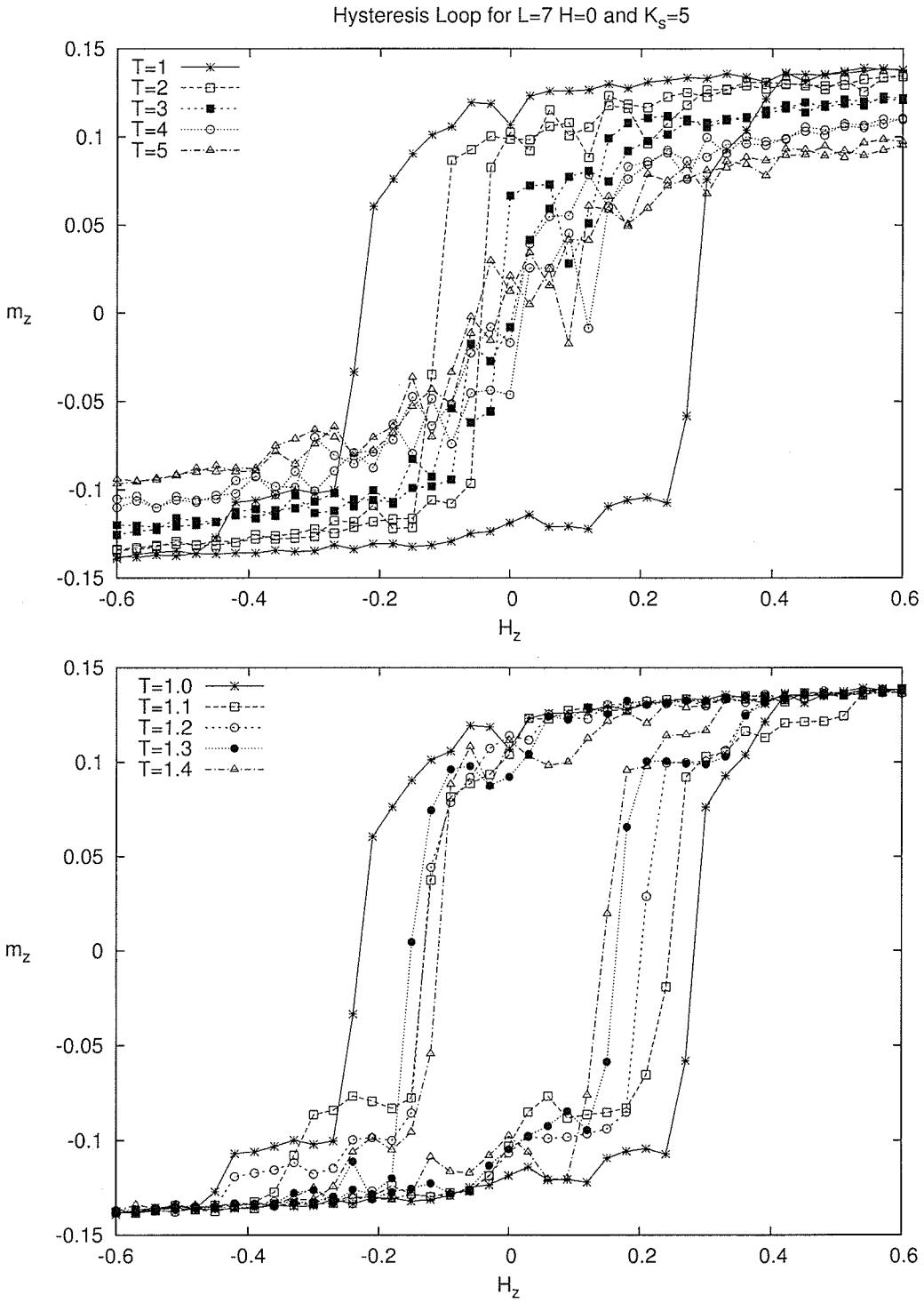

Figure 5.12: Hysteresis loop for $L = 7$ and $K_s = 5$ in the zero field cooled case. The upper panel shows the z-component of the total magnetization as a function of the applied field in the range $1 \leq T \leq 5$. The lower panel shows the behaviour over a narrower temperature range.

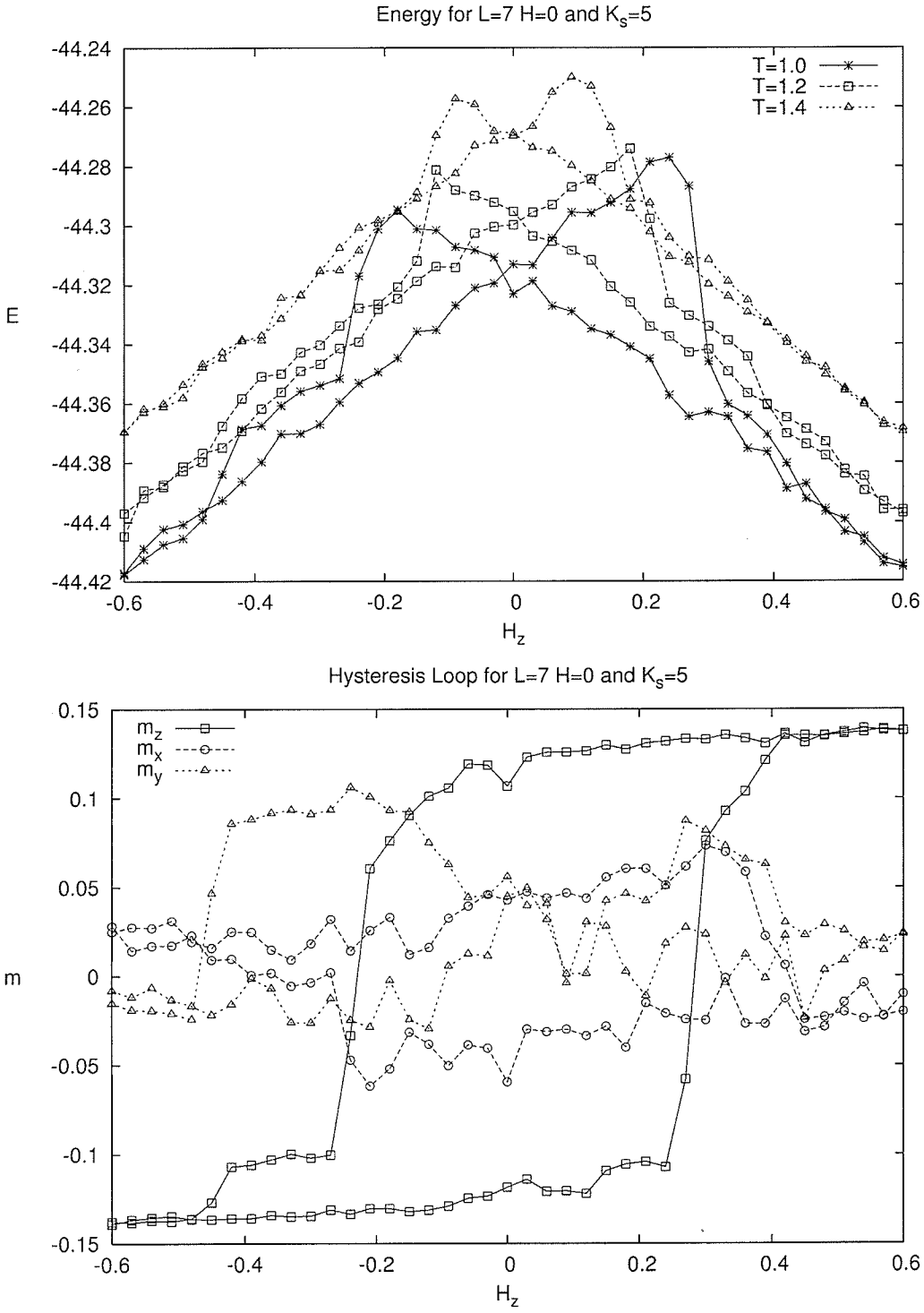

Figure 5.13: The energy per particle as a function of the applied field (upper panel) for the hysteresis loops shown in Fig. 5.12 and the three components of the total magnetization (lower panel) at the lowest temperature $T = 1$.

A second abrupt decrease occurs near $H_z \sim -0.4$. These abrupt decreases indicate the limits of metastable configurations of the particle as the applied field is changed. As the temperature increases, the size of the abrupt energy jumps decrease and their location moves towards $H_z = 0$. The lower panel of the figure shows the behaviour of all three components of the magnetization as the loop is traversed at $T = 1$. The components perpendicular to the applied field grow somewhat as the magnitude is decreased until near $H_z \sim -0.2$. At this point, the component parallel to the field changes sign but the component perpendicular becomes large indicating that only partial reversal occurs with the magnitude of the components along the field and perpendicular to it approximately equal until $H_z \sim -0.4$ where complete reversal finally occurs. Hence the reversal appears to be a two step process.

Fig. 5.14 shows the hysteresis loops for a particle which has been cooled in a field $H = 5$ applied in the z-direction. The behaviour is very similar to that in the zero-field cooled case shown in Fig. 5.12 except that the hysteresis loop appears to have a small shift to the left and is no longer symmetric about $H_z = 0$. This feature indicates that a small amount of exchange bias may be present. Fig. 5.15 shows the energy per particle and all three components of the total magnetization as the hysteresis loop is traveresed. The reversal appears to be a 2-step process in this case as well. This behaviour is not characteristic of a single domain particle.

Fig. 5.16 shows the z-component of the core and surface magnetizations as the hysteresis loop is traversed at $T = 1$ for both the zero and non-zero field cooled cases. Both the core and surface exhibit the two stage reversal process for this value of K_s. This suggests that the particle reversal is quite different from a single domain reversal mechanism where the core reversal occurs separately and is affected by the surface. On the contrary, different regions of the particle have their core and surface acting together at two different reversed fields.

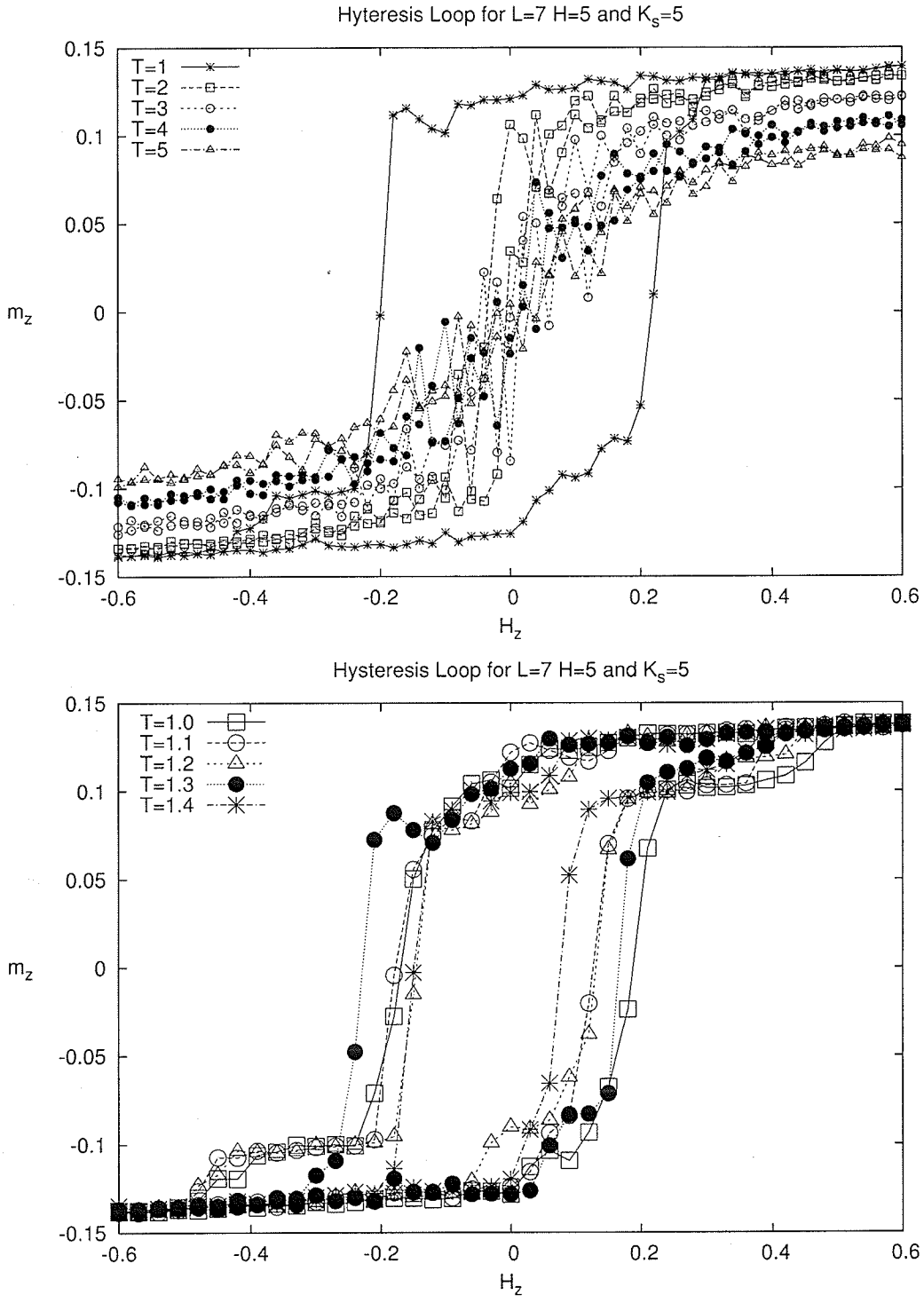

Figure 5.14: Hysteresis loop for $L = 7$ and $K_s = 5$ in the non-zero field cooled case. The upper panel shows the z-component of the total magnetization as a function of the applied field in the range $1 \leq T \leq 5$. The lower panel shows the behaviour over a narrower temperature range.

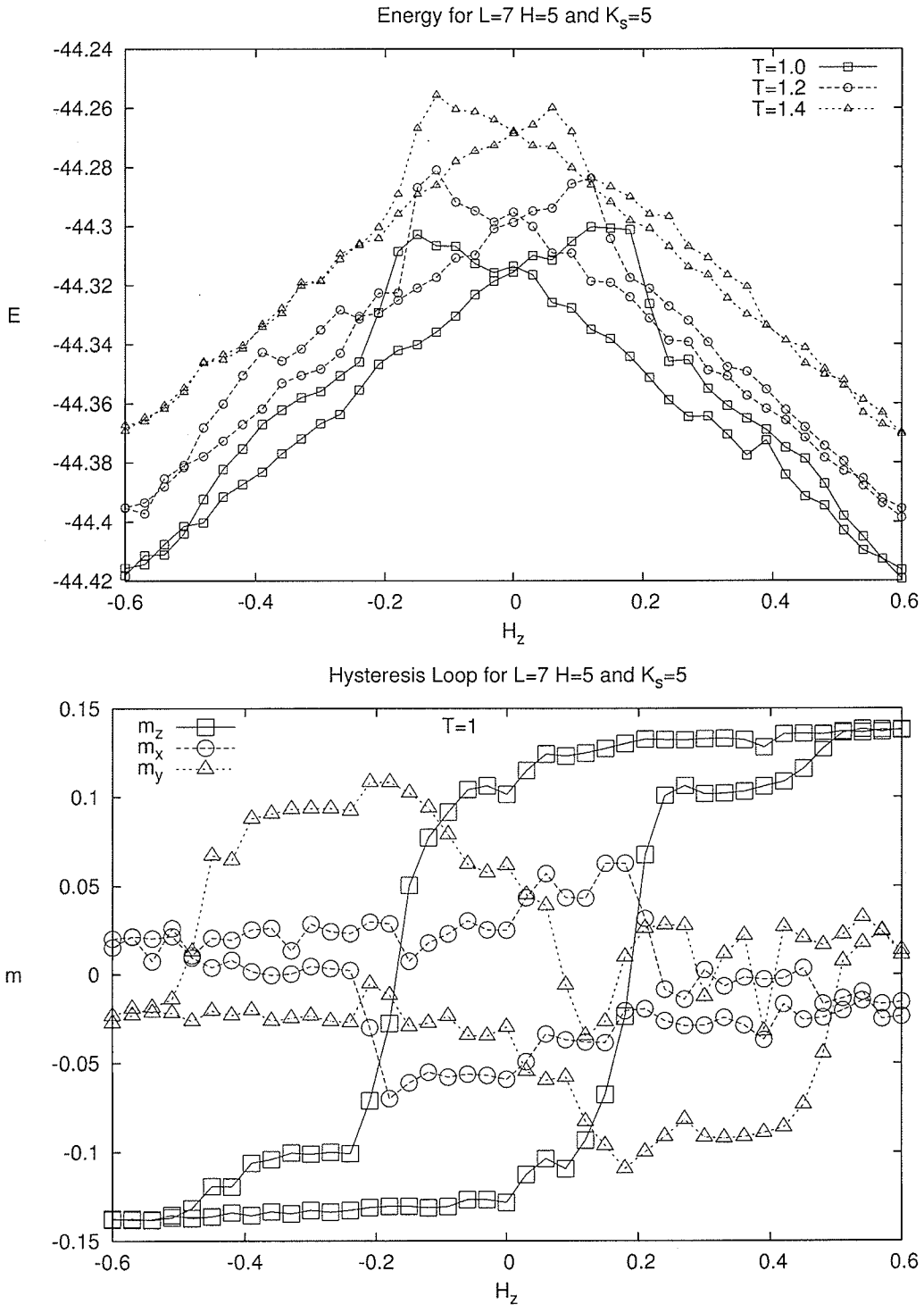

Figure 5.15: The energy per particle as a function of the applied field (upper panel) for the hysteresis loops shown in Fig. 5.14 and the three components of the total magnetization (lower panel) at the lowest temperature $T = 1$.

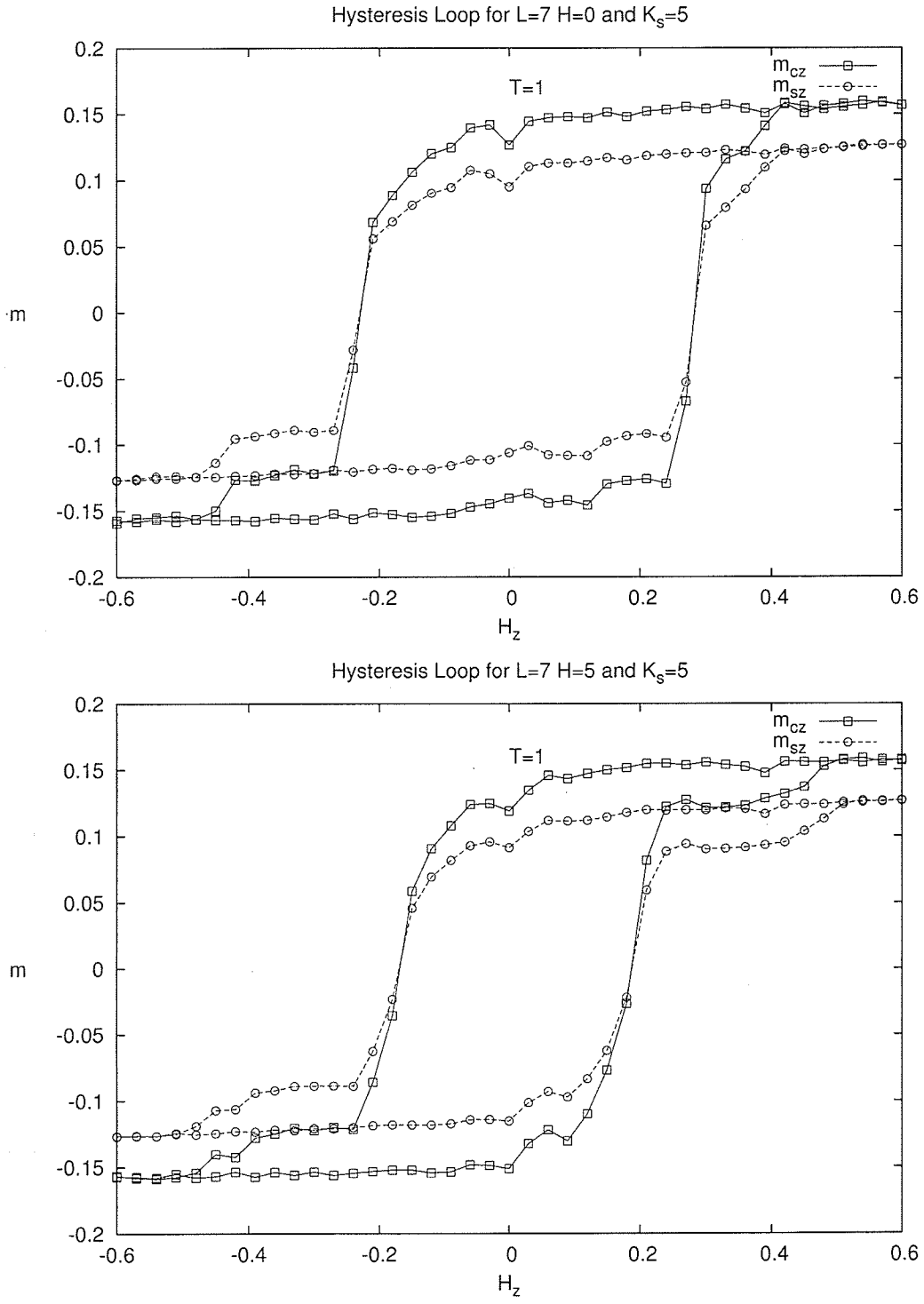

Figure 5.16: Hysteresis loops of the zero field (upper panel) and non-zero field (lower panel) cooled cases for the core and surface magnetizations at the lowest temperature $T = 1$.

We have also studied the hysteresis properties for smaller and larger values of the surface anisotropy constant K_s. Fig. 5.17 shows the hysteresis loop for $L = 7$ and $K_s = 1$ in the field cooled case. The upper panel shows the z-component of the total magnetization as a function of H_z for several temperatures. The particle exhibits superparamagnetic behaviour consistent with the blocking temperature estimated previously to be $T_B \sim 0.5$. The lower panel shows the components of the magnetization which indicate that the net moment of the particle simply follows the applied field.

Fig. 5.18 shows results for $L = 7$ and $K_s = 10$ after cooling in a field. The upper panel shows m_z at several low temperatures where a large coercivity is present. The two step reversal process found for $K_s = 5$ now seems to be replaced by a continuous process which occurs over a wide range of reversal fields. The lower panel shows the total magnetization components at $T = 1$. The components transverse to the field direction grow in the region where reversal of the parallel component occurs but they do not exhibit the plateaus observed in the case $K_s = 5$. Fig. 5.19 shows the energy per particle as a function of H_z for $K_s = 1$ (upper panel) and $K_s = 10$ (lower panel) at $T = 1$. For $K_s = 1$, there are no metastable branches whereas there are large regions of metastability for $K_s = 10$. The jumps in energy from the metastable to stable branches is less abrupt than in the case $K_s = 5$. However, there is some evidence for a two step reversal process in the range where the magnitude of the applied field is between 2 and 4. Fig. 5.20 shows the hysteresis loop for both the core and surface magnetizations when $K_s = 10$ at the lowest temperature $T = 1$. In contrast to Fig. 5.16, the core and surface magnetizations reverse at different fields. As the applied field is reduced from it's maximum value, the surface magnetization decreases linearly until the point where the core magnetization changes sign. This is followed by another linear region which has a much larger slope. Hence, for larger values of the surface anisotropy, the reversal of the particle's magnetization again appears to be a two stage process but it is quite different from that at smaller values of K_s.

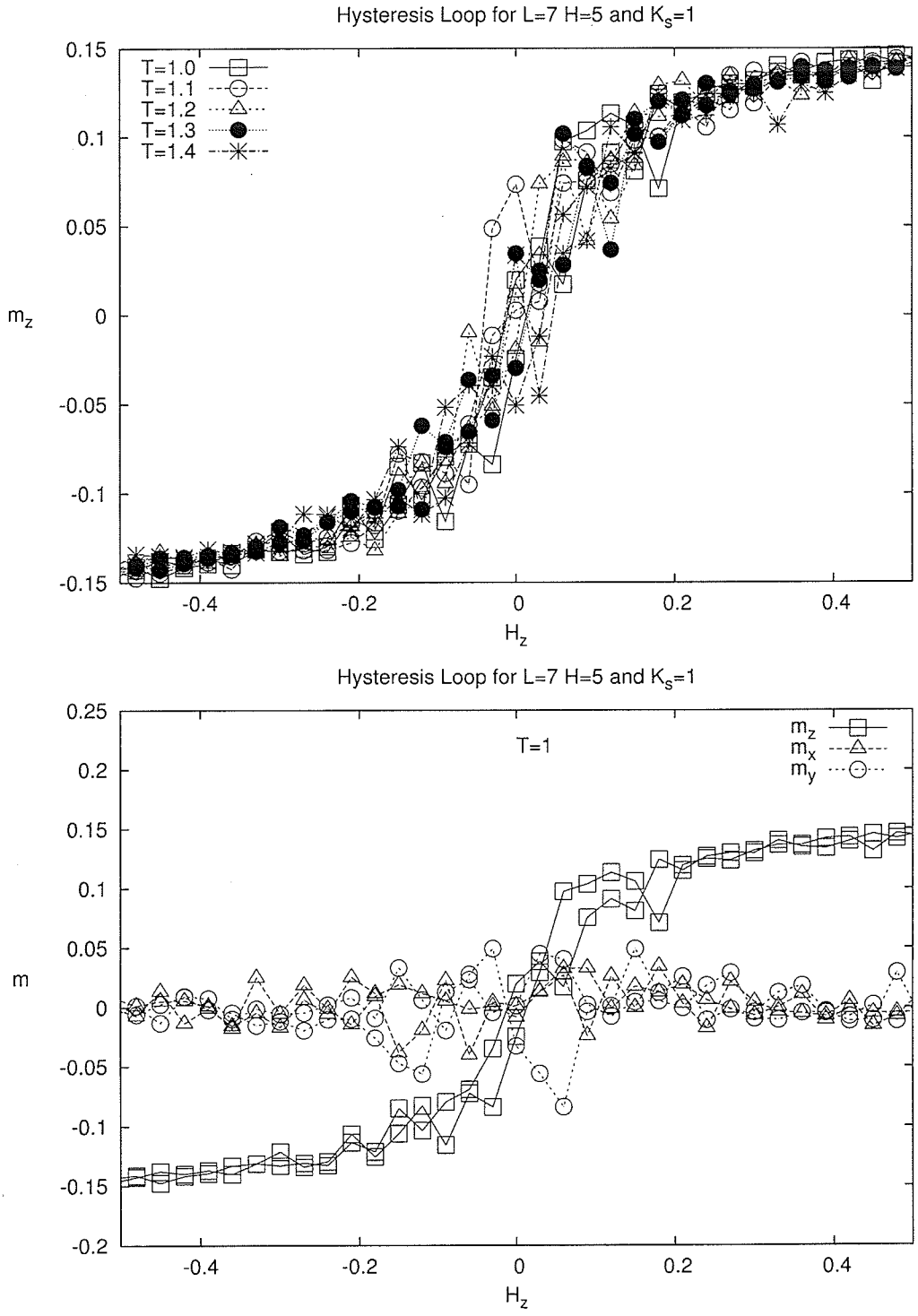

Figure 5.17: Hysteresis loops for $L = 7$ and $K_s = 1$ at low temperatures (upper panel) in the field cooled case and the three components of the total magnetization at $T = 1$.

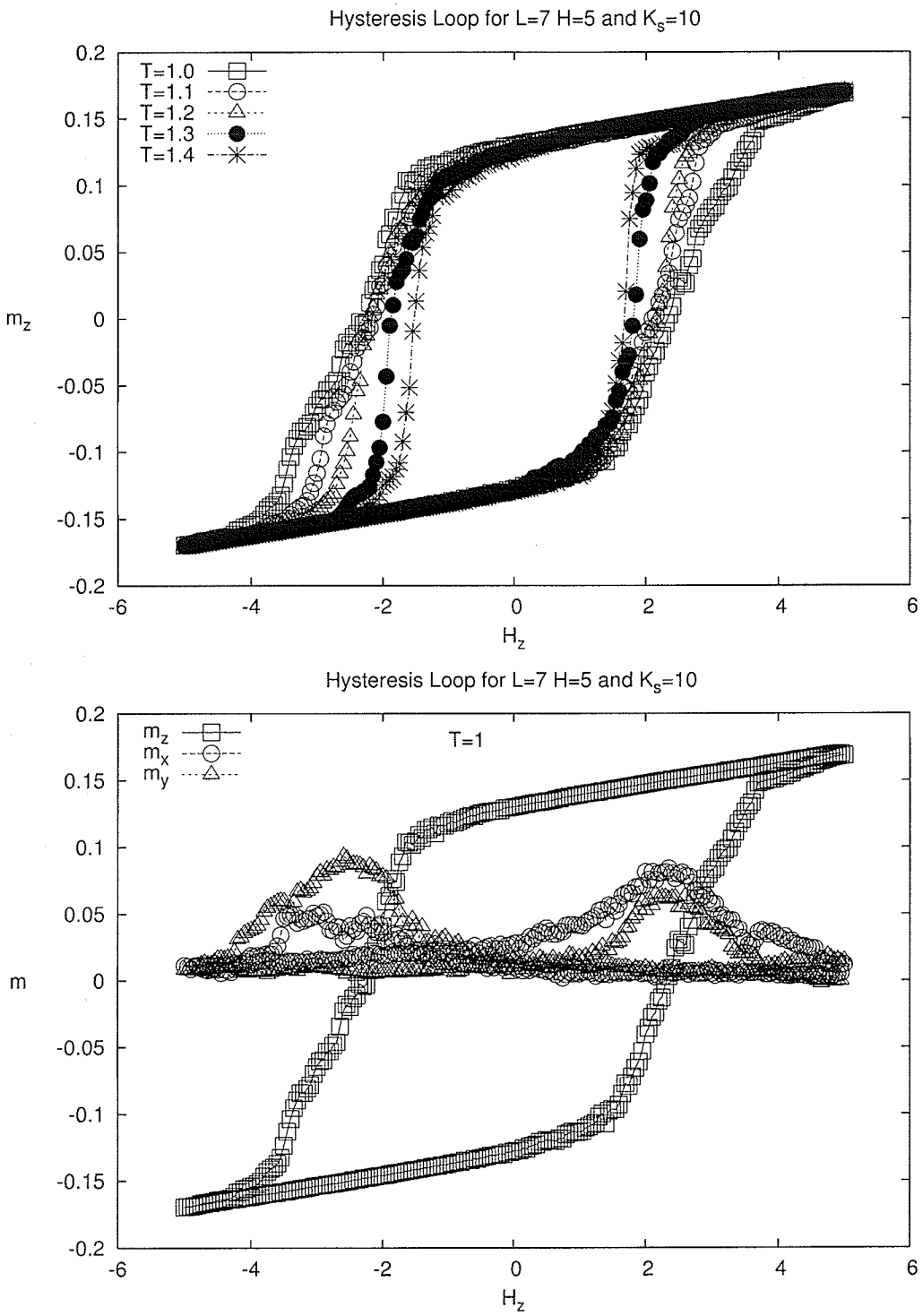

Figure 5.18: Hysteresis loops for $L = 7$ and $K_s = 10$ at low temperatures (upper panel) in the field cooled case and the three components of the total magnetization at $T = 1$.

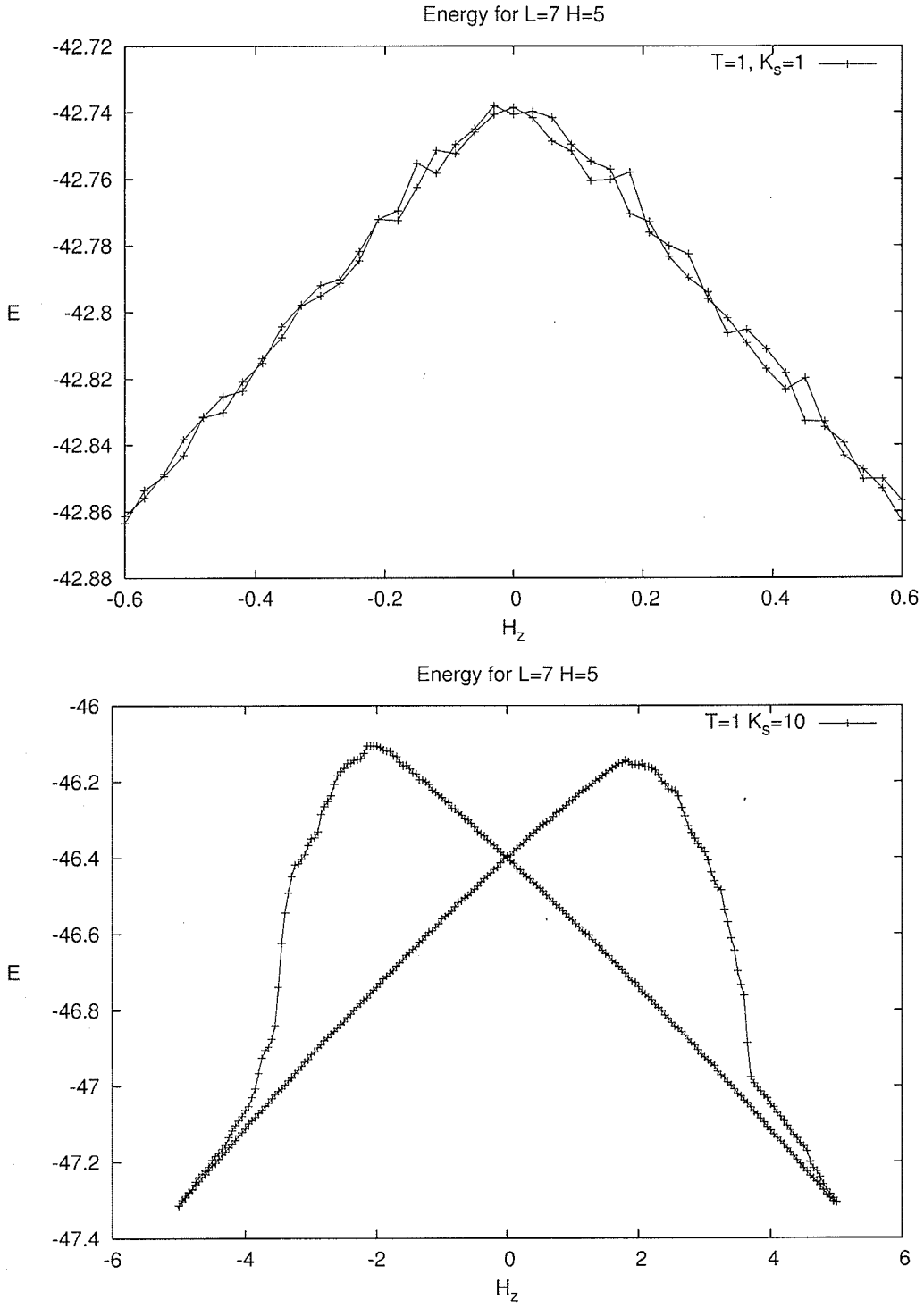

Figure 5.19: Energy per particle as a function of the applied field at $T = 1$ for $K_s = 1$ (upper panel) and $K_s = 10$ (lower panel) for the loops in Figs. 5.17 and 5.18.

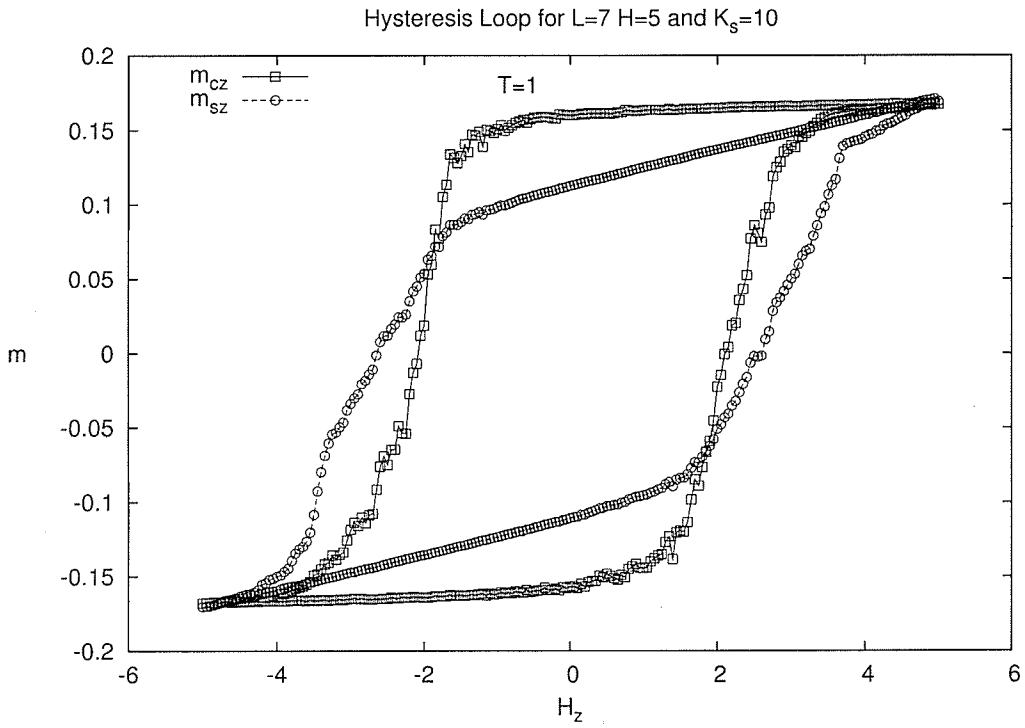

Figure 5.20: Hysteresis loops for the core and surface magnetizations when $L = 7$ and $K_s = 10$.

Fig. 5.21 illustrates schematically the two stage reversal process for the case $K_s = 5$. In frame (a), the core and surface magnetizations are polarized in the direction of the applied field. As the field is reduced and reversed as in frame (b), the magnetizations of both the core and surface in the equatorial region of the particle develop components perpendicular to the field. Note that the figure is a cut through the particle in the $x - z$ plane. Since the anisotropy favors the moments to be normal to the surface, it is this region which can overcome the applied field first. As the field is reversed further as in frame (c), the core and surface spins in the polar regions reverse but the equatorial regions maintain a large transverse component. Finally in frame (d), the core and surface magnetizations are polarized in the reverse direction. Similar reversal processes have been reported by Berger et. al. [54]

Fig. 5.22 shows a similar picture for the case when $K_s = 10$. Stages (a) and (d) are the same as in the previous case but stages (b) and (c) are different. In (c), the core magnetization reverses but the surface magnetization does not. The surface magnetization reverses when the applied field is reduced further as in (d).

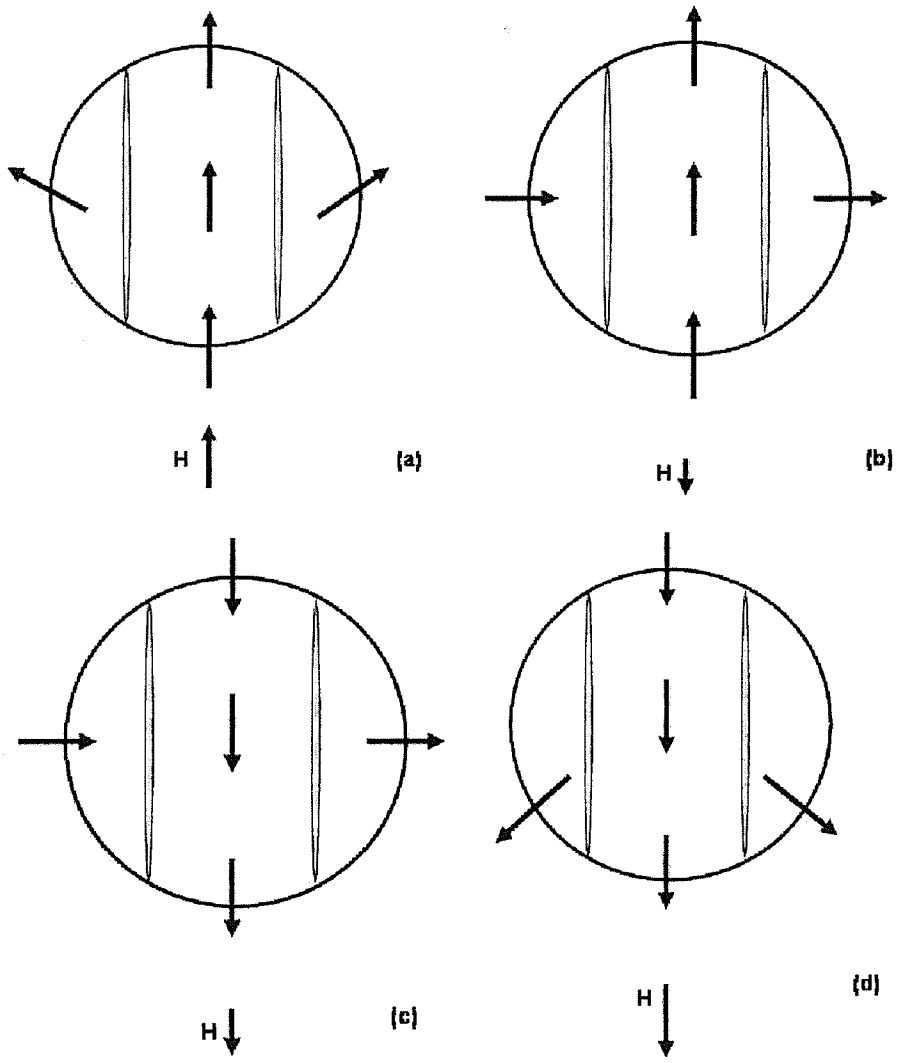

Figure 5.21: Schematic description of the magnetization reversal process for $K_s = 5$.

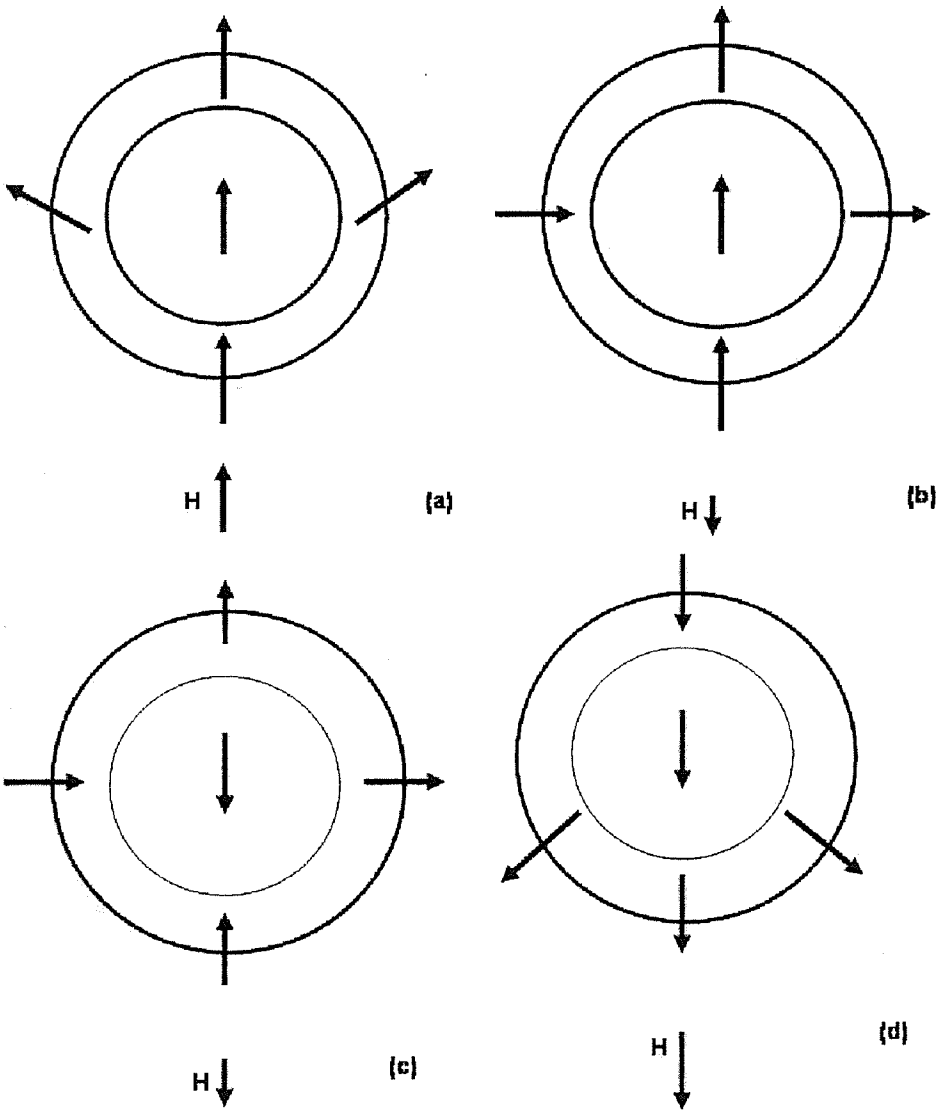

Figure 5.22: Schematic description of the magnetization reversal process for $K_s = 10$.

5.4 *Coercivity and Exchange Bias*

Using the results obtained for the hysteresis loops, we have determined the left and right coercive fields, h_1 and h_2, respectively as a function of temperature. These fields correspond to the field values where the total magnetization of the particles changes sign. The behaviour is similar for all particle sizes but does depend on the value of the surface anisotropy constant. This is perhaps not unexpected since the blocking temperatures where independent of particle size but increased as the surface anisotropy was increased.

Fig. 5.23 shows the left and right coercive fields as a function of temperature for size $L = 7$ and $K_s = 5$ for both the zero field cooled (upper panel) and non-zero field cooled (lower panel) cases. There are large fluctuations of the field values with temperature but the fields rapidly approach zero as T increases towards the blocking temperature $T_B \sim 3.0$ in both cases. The coercivity H_c and the exchange bias H_{ex} are obtained from h_1 and h_2 using eqn. 2.27 and these are shown in Fig. 5.24. The upper panel is the zero field cooled case and the lower panel is the field cooled particle. In both cases, there is no appreciable exchange bias present and the coercivity behaves similarly in both cases. In neither case does the behaviour correspond to that in equation 2.25 for a single domain particle. The coercivity decreases quite rapidly with T and can be fit reasonably well by the form

$$H_c(T) = a\ exp(-T/b) \tag{5.5}$$

where for the zero field cooled case we find $a = 1.10 \pm 0.27$ and $b = 0.64 \pm 0.09$ and for the non-zero field cooled case $a = 0.46 \pm 0.18$ and $b = 1.14 \pm 0.41$. This functional form is the same as that used to fit the surface magnetization temperature dependence for this particle.

Fig. 5.25 shows the left and right coercive fields (upper panel) and the corresponding coercive and exchange bias fields (lower panel) for the field cooled particle with $L = 7$ and $K_s = 10$. The zero field cooled particle behaves almost identically.

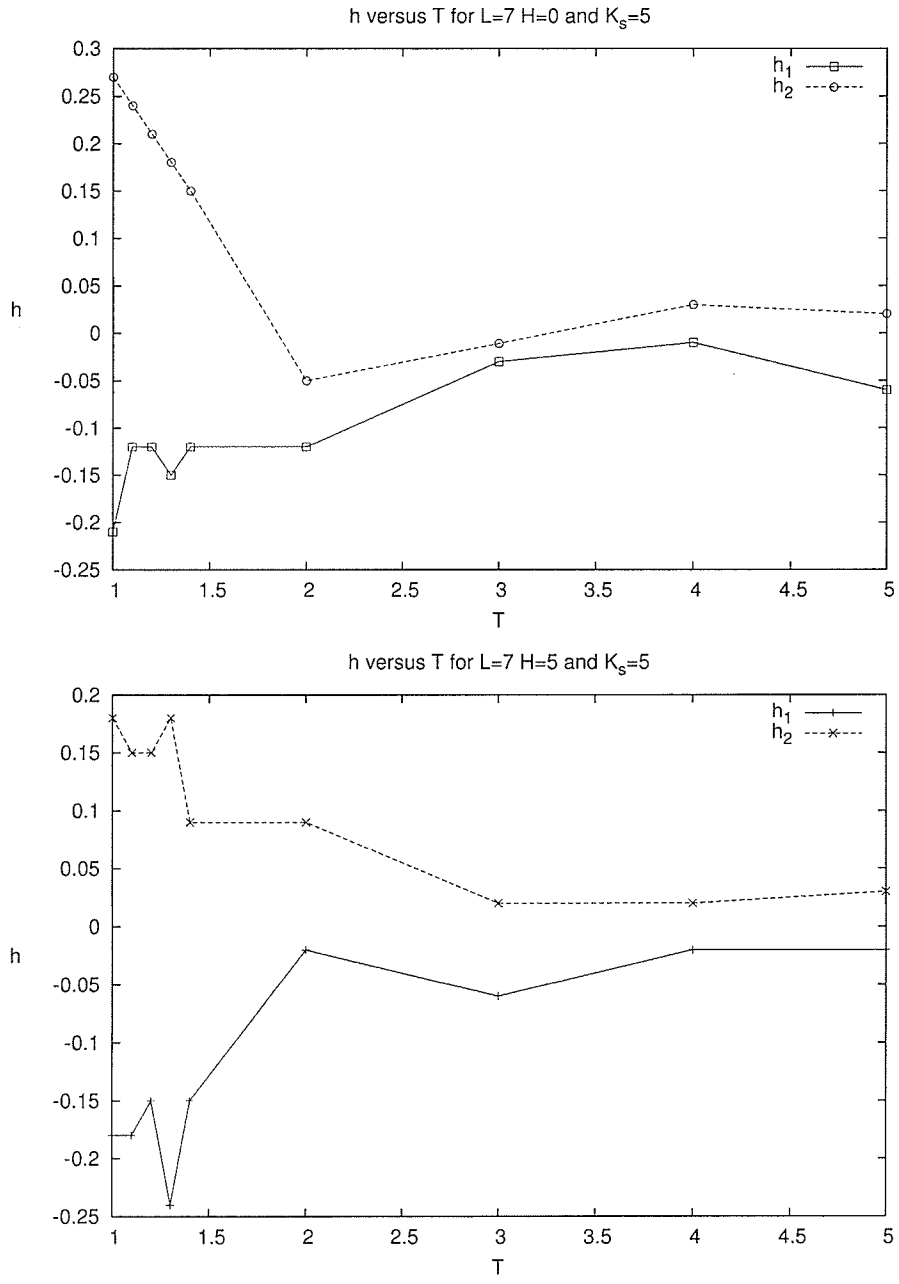

Figure 5.23: Left (h_1) and right (h_2) coercive fields as a function of temperature for the zero field (upper panel) and non-zero field (lower panel) cooled cases with $L = 7$ and $K_s = 5$.

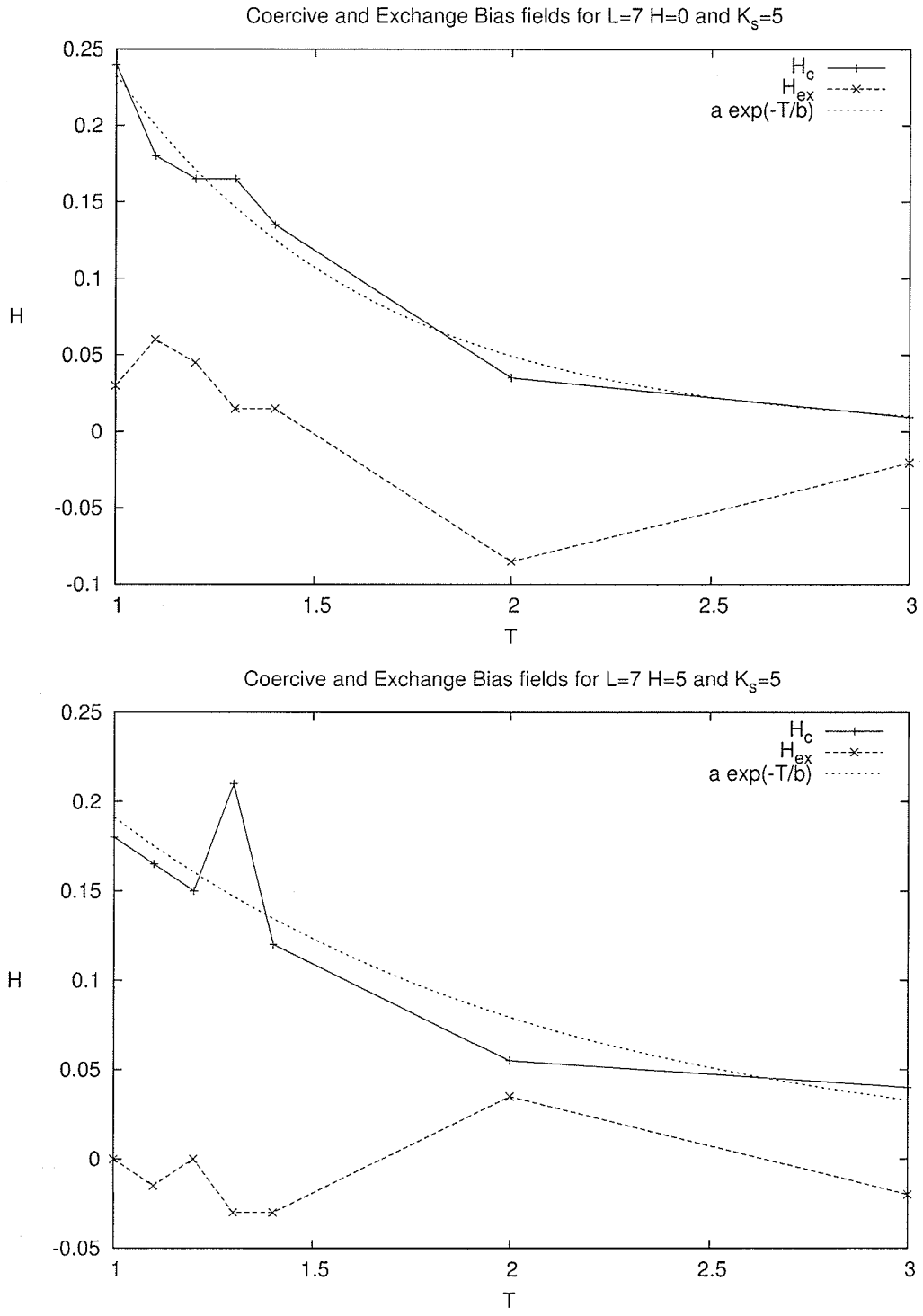

Figure 5.24: Coercive field ($H_c = (h_2 - h_1)/2$) and exchange bias field ($H_{ex} = (h_2 + h_1)/2$) as a function of temperature for the zero field (upper panel) and non-zero field (lower panel) cooled cases of Fig. 5.21 .

The coercivity is a factor of ten larger than in the $K_s = 5$ case shown in figure 5.24. There is no evidence of exchange bias for this case and the temperature dependence of H_c cannot be fit to the forms in equations 2.25 or 5.5. However, the modified form

$$H_c(T) = a\ exp(-(T/b)^n) \tag{5.6}$$

yields a reasonable fit with $a = 2.31 \pm 0.18$, $b = 1.58 \pm 0.11$ and $n = 8.28 \pm 5.37$. This functional form is the same as that used to describe the surface magnetization for particles with $K_s = 10$.

Our results for all particle sizes with $L = 4, 5, 6, 7, 8, 9$ do not show any significant exchange bias. The surface anisotropy constant K_s influences strongly the magnitude of the coercivity and its temperature dependence.

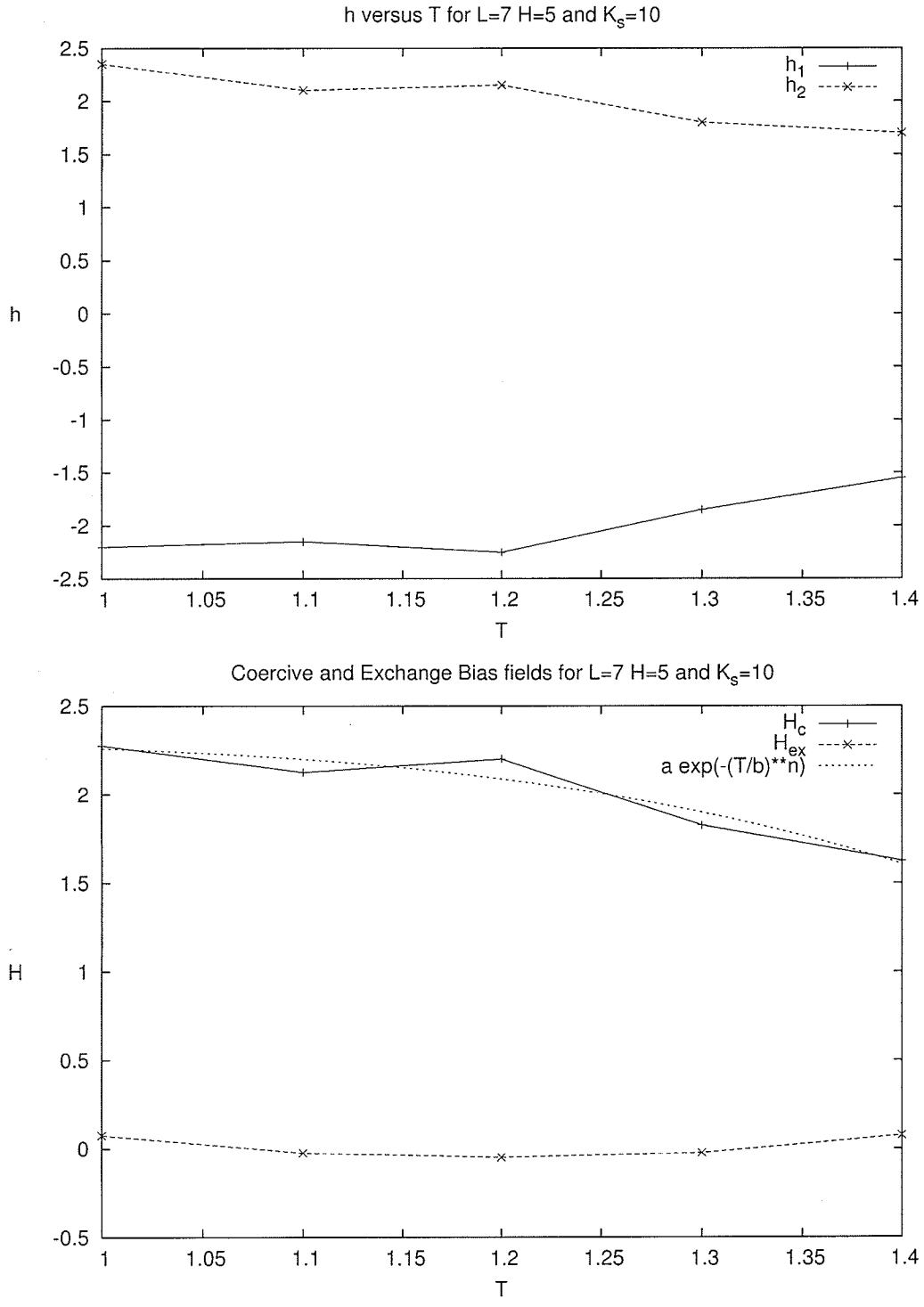

Figure 5.25: Left (h_1) and right (h_2) coercive fields (upper panel) as a function of temperature for the non-zero field cooled case with $L = 7$ and $K_s = 10$ and the corresponding coercive and exchange bias fields (lower panel).

Chapter 6

SUMMARY AND FUTURE WORK

6.1 Summary

In this thesis we have used Monte Carlo methods to study the magnetic properties of maghemite nanoparticles. The experimental properties and simplified model that we used to describe the particles were discussed in chapter 3. The particles have a spinel structure with a spherical geometry. There are core spins at the center of the particles and surface spins surrounding them with oxygen vacancies distributed throughout. The exchange interactions have their bulk values in the core but smaller values in the surface region and at the core-surface interface. The anisotropy in the core also has its bulk value but the surface anisotropy constant had a range of larger values. Our temperature scale is approximately a factor of ten smaller than the experimental temperature scale since we use spins of unit magnitude.

The Monte Carlo method was described in detail in chapter 4. The method is a modified version of the usual heat bath method used to study classical spins to allow for the finite length of the Fe spins in maghemite. The modifications only affect the behaviour of the thermodynamic quantities at low temperatures where classical models fail. Chapter 5 describes our results for the temperature dependence of the total, core and surface magnetizations for various particle sizes and values of the surface anisotropy constant. At high temperatures $T_c \sim 70$ the core spins begin to develop a ferrimagnetic order with a net moment. However, the direction of the moment is fluctuating and the particle exhibits superparamagnetic behaviour down to much lower temperatures. The surface spins do not develop ferrimagnetic order

until a much lower temperature $T_s \sim 5$. The net moment of the particle continues to fluctuate until the blocking temperature $T_B \sim 3$ is reached and a coercivity develops. The temperature dependence of the surface magnetization obtained from our Monte Carlo results is very similar to that observed experimentally.

Both the surface ordering temperature and the blocking temperature do not depend on the size of the nanoparticle. However, they both increase approximately linearly with the surface anisotropy constant K_s. When the particles are cooled in a non-zero applied field, the magnetizations increase. The largest change occurs for the surface magnetization. Hysteresis loops were studied in both the zero field and non-zero field cooled cases. The differences in the loops for these different cooling histories were quite small. Experimental systems exhibit a shift of the hysteresis loop when cooled in a field. This shift corresponds to an exchange bias field. We find no evidence of exchange bias in our model.

The surface anisotropy has a strong effect on the hysteresis loops and the nature of the moment reversal of the particles. For small values of K_s, the blocking temperature is reduced significantly and the hysteresis loops only display superparamagnetic behaviour with no coercivity. The particles reverse their magnetization by following the field direction. For intermediate values of K_s, the blocking temperature is increased and the hysteresis loops exhibit coercivity. There is a main loop as well as minor loops. The reversal of the moment appears to be a two stage process. The temperature dependence of the coercivity appears to be similar to that of the surface magnetization with an approximate exponential form. At large values of the surface anisotropy, the blocking temperature is increased again and the hysteresis loops exhibit a ten-fold increase in the coercivity. The minor loops are merged with the main loop and the moment reversal occurs in two steps with the core spins reversing first followed by the surface spins.

6.2 Future Work

The results presented here are a first attempt at studying the magnetic properties of nanoparticles. Some of the results agree qualitatively with recent experiments but others do not. The absence of exchange bias in our model could be due to the fact that our model is too simple or it could be due to our Monte Carlo algorithm. Further work could include modifying the model or the algoritm or both. One of the problems with our calculations is that they require a great deal of cpu time. Each hysteresis loop uses 30,000 mcs for each of 200 field values at a single temperature which typically requires 24 hours to complete. Parallelization of the code could speed up this process significantly and allow us to vary both the exchange parameters and applied field strengths over a wider range.

BIBLIOGRAPHY

[1] A. H. Morrish. *The Physical Principles of Magnetism.* John Wiley and Sons, Inc, 1965.

[2] S. Chikazumi. *Physics of Magnetism.* John Wiley and Sons, Inc, 1964.

[3] K.H.J. Buschow and F.R. De Boer. *Physics of Magnetism and Magnetic Materials.* Kluwer Academic and Plenum Publishers, New York, 2003.

[4] F. Brailsford. *Physical Principles of Magnetism.* D. Van Nostrand Company Ltd, 1966.

[5] Mathias Getzlaff. *Fundamentals of Magnetism.* Springer, 2008.

[6] P.A.M. Dirac. *Proc. Roy. Soc.*, **A112**:661, 1926.

[7] W. Heisenberg. *Z. Physik 38*, **6-7**:411, 1926.

[8] H. A Kramers. *Physica*, **1**:182, 1934.

[9] P. W Anderson. *Phys. Rev.*, **79**:350, 1950.

[10] J.H. Van Vleck. *J. Phys. Radium*, **12**:262, 1951.

[11] R.N Stuart and W. Marshall. *Proc. Phys. Soc.*, **87**:749, 1966.

[12] M. A Ruderman and C. Kittel. *Phys. Rev.*, **96**:99, 1954.

[13] F. Bloch. *Z. Physik*, **74**:295, 1932.

[14] L. Néel. *Compt. rend.(Paris)*, **228**:604, 1949.

[15] L. Néel. *Ann. Geophys.*, **5**:99, 1949.

[16] E. C. Stoner and E. P. Wohlfarth. *Phil. Trans. Roy. Soc. (London)*, **A-240**:599, 1948.

[17] W. H. Meiklejohn and C. P. Bean. *Phys. Rev.*, **102**:1413, 1956.

[18] W. H. Meiklejohn and C. P. Bean. *Phys. Rev.*, **105**:904, 1957.

[19] William Fuller Brown Jr. and Clarke E. Johnson Jr. *J. Appl. Phys.*, **33**:2752, 1962.

[20] G.M. da Costa, E. de Grave, and R.E Vandenberghe. *Hyperfine Interact.*, **117**:207, 1998.

[21] Radek Zboril, Miroslav Mashlan, and Dimitris Petridis. *Chem.Mater.*, **14**:969, 2002.

[22] J. Tűcek and R. Zboril. *Czechoslovak Journal of Physics*, **55**:893, 2005.

[23] J. Tűcek, Radek Zboril, and Dimitris Petridis. *J. Nanosci. Nanotechnol.*, **6**:926, 2006.

[24] J.M.D. Coey. *Phys. Rev. Lett.*, **27**:1140, 1971.

[25] A. Millan, A.Urtizberea, N.J.O. Silva, F.Palacio, V.S. Amaral, E. Snoeck, and V. Serin. *J.Magn.Magn.Mater.*, **312**:L5, 2007.

[26] T.N. Shendruk, R.D. Desautels, B.W. Southern, and J. van Lierop. *Nanotechnology*, **18**:455704, 2007.

[27] R.H. Kodama and A.E Berkowitz. *Phys. Rev. B.*, **59**:6321, 1999.

[28] R.H. Kodama and A.E. Berkowitz. *Phys. Rev. Lett.*, **77**:394, 1996.

[29] S.Mørup, F. Bødker, P.V. Hendriksen, and S. Linderoth. *Phys. Rev. B.*, **52**:287, 1995.

[30] J. Restrepo, Y. labaye, and J.M. Greneche. *Revista Colombiana De Fisica*, **38**:1559, 2006.

[31] J. Restrepo, Y. labaye, and J.M. Greneche. *Revista Colombiana De Fisica*, **39**:183, 2007.

[32] J. Restrepo, Y. labaye, and L. Berger J.M. Greneche. *J. Magn.Magn.Mater.*, **272-276**:681, 2004.

[33] J. Restrepo, Y. labaye, and J.M. Greneche. *Physica B*, **384**:221, 2006.

[34] M. Metropolis, A. W. Rosenbluth, M. N. Rosenbluth, A. H. Teller, and E. Teller. *J. Chem. Phys.*, 21:1087, 1953.

[35] E. Eftaxias and K.N. Trohidou. *Phys. Rev. B*, **71**:134406, 2005.

[36] K.N. Trohidou, M. Vasilakaki, L. Del Bianco, D. Fiorani, and A.M. Testa. *J.Magn.Magn.Mater.*, **192**:203, 1999.

[37] Marianna Vasilakaki and Kalliopi N Trohidou. *J.Phys.D:Appl.Phys.*, **41**:134006, 2008.

[38] Òscar Iglesias, Xavier Batlle, and Amícar Labarta. *J.Phys.D:Appl.Phys.*, **41**:134010, 2008.

[39] Òscar Iglesias, Xavier Batlle, and Amícar Labarta. *Phys. Rev. B*, **72**:212401, 2005.

[40] Òscar Iglesias and Amícar Labarta. *Phys. Rev. B*, **63**:184416, 2008.

[41] Òscar Iglesias and Amícar Labarta. *Phys. stat.sol.*, **1**:3481, 2004.

[42] H. KachKachi, A. Ezzir, M.Nogues, and E.Tronc. *Eur. Phys. J. B*, **14**:681, 2000.

[43] E. De Biasi, C.A. Ramos, R.D. Zysler, and D. Fiorani. *Physica B*, **372**:345, 2006.

[44] J. Mazo-Zuluaga, J. Restrepo, and J. Mejía-López. *J. Appl. Phys.*, **103**:113906, 2008.

[45] J. Mazo-Zuluaga, J. Restrepo, and J. Mejía-López. *Physica B*, **398**:187, 2007.

[46] J. Mazo-Zuluaga, J. Restrepo, and J. Mejía-López. *J. Phys.:Condens.Matter*, **20**:195213, 2008.

[47] N.A. Usov and Yu. B. Grebenshchikov. *J. Appl. Phys.*, **104**:043903, 2008.

[48] D. P. Landau and Kurt Binder. *A Guide to Monte Carlo Simulations in Statistical Physics.* Cambridge University Press, 2000.

[49] M.E.J.Newman and G.T. Barkema. *Monte Carlo Methods in Statistical Physics.* Clarendon Press Oxford, 1999.

[50] U.Burghaus, J. Stephan, L.Vattuone, and J.M. Rogowska. *A practical Guide to Kinetic Monte Carlo Simulations and Classical Molecular Dynamics Simulations.* Nova Science Publishers,inc. Newyork, 2005.

[51] K. Binder and D.W Heermann. *Monte Carlo Simulation in Statistical Physics An Introduction.* Springer, 2002.

[52] Y Miyatake, M Yamamoto, J.J. Kim, M. Toyonaga, and O.Nagai. *J.Phys.C:Solid State Phys.*, **19**:2539, 1986.

[53] L. W. Lee and A.P. Young. *Phys. Rev. B*, **76**:024405, 2007.

[54] L. Berger, Y. Labaye, M. Tamine, and J. M. D. Coey. *Phys. Rev. B*, **77**:104431, 2008.